Structural Mechanism of A RISC-Loading Complex

Na Cao[1, 3], Jia Wang[1, 2, 3] *, Hong-Wei Wang[1] *

1 Ministry of Education Key Laboratory of Protein Sciences, Tsinghua-Peking Joint Center for Life Sciences, Beijing Advanced Innovation Center for Structural Biology, Beijing Frontier Research Center of Biological Structures, School of Life Sciences, Tsinghua University, Beijing, 100084, China.

2 Biomedical Basic Research Center (BBRC) of Jiangsu Province, MOE Key Laboratory of Geriatric Diseases and Immunology, Institute of Molecular Enzymology, School of Life Sciences, Suzhou Medical College of Soochow University, Suzhou, Jiangsu, 215123, China.

3 These authors contributed equally: Na Cao and Jia Wang

* Corresponding authors:, Jia Wang (wj@suda.edu.cn), Hong-Wei Wang (hongweiwang@tsinghua.edu.cn)

Abstract

In the RNAi pathway, small RNAs processed by Dicer are loaded into Argonaute proteins to form the RNA-induced silencing complex (RISC), which silences target genes. The intermediate complex responsible for this transfer is known as the RISC-loading complex (RLC). However, the molecular mechanism of this delivery process and the identity of all required components have remained elusive. Here we determined the cryo-EM structure of the RISC-loading complex in the *Drosophila* siRNA pathway. Our high-resolution structural analysis reveals that multiple domains, including the RIIIai of Dicer-2 and the dsRBDs of R2D2, play critical roles in loading the siRNA duplex into Ago2. The Hsp90 machinery reorganizes the spatial arrangement of Ago2 domains, maintaining Ago2 in an open conformation to receive the nascent siRNA duplex. Furthermore, this structure uncovers the mechanism of siRNA strand selection. During loading, the strand whose 5′ end is anchored in the Dicer-2 Platform-binding pocket is everted – a process facilitated by R2D2 – allowing its 5′ end to engage the binding pocket in the MID domain of Ago2. This strand becomes the guide strand in the mature RISC.

Introduction

RNA interference (RNAi) has emerged as a powerful reverse genetics tool due to its conservation and ability to regulate gene expression[1-6]. The effector of the RNAi pathway is the RNA-induced silencing complex (RISC), which typically contains an Argonaute family protein and a single-stranded small RNA of about 20-23 nt (guide strand)[7,8]. The guide strand in RISC directs Argonaute and other components to target transcripts by base pairing, resulting in gene silencing through translational repression or RNA degradation[9-13]. RISC-mediated silencing plays a key role in fine-tuning protein-coding gene expression and can contribute to immune responses against viral infections and transposons, though the antiviral role of RNAi varies among organisms[14].

Small RNAs can be classified by their processing and maturation pathways as siRNAs, miRNAs, and piRNAs[15,16]. While siRNAs and miRNAs load into Ago-family

proteins to form RISC with guide strands, piRNAs associate with PIWI-clade Argonaute proteins and often follow distinct maturation pathways[17-19]. Both siRNAs and miRNAs are processed from precursor RNAs with double-stranded property by Dicer, a member of the RNase III family[20-24]. The precursors are: long double-stranded RNAs (dsRNAs) for siRNAs, and hairpin-structured precursors (pre-miRNAs) for miRNAs. Dicer processes these precursors into small RNA duplexes of ~21-23 bp, which are subsequently delivered to Argonaute proteins and unwound to release the passenger strand, leaving the guide strand stably bound to the Argonaute protein to form the mature, functional RISC[7,25-27]. This loading and maturation sequence is commonly referred to as RISC loading.

Existing cellular and biochemical studies have demonstrated that a multi-component protein-nucleic acid complex can form during the transition from Dicer-mediated process of mature double-stranded small RNAs to their delivery and loading onto Argonaute proteins; this complex is commonly referred to as the RISC-loading complex (RLC)[28-30]. In vitro experiments have shown that the core components of the human RLC - Dicer, TRBP, and Ago2 - can reconstitute the small RNA loading process[31,32]. In *Drosophila*, RISC loading appears to be mediated by multiple complexes, with composition and mechanisms varying by the small RNA type[33,34].

In *Drosophila*, two Dicer enzymes generate distinct small RNAs: Dicer-1 processes miRNA precursors, while Dicer-2 processes dsRNA into siRNA duplexes[35,36]. Primary miRNAs (pri-miRNAs) are first cleaved in the nucleus by Drosha and its cofactor Pasha (the human homolog is DGCR8) to produce hairpin-structured pre-miRNAs of approximately 65-70 nt[37,38]. In the cytoplasm, pre-miRNAs are processed by Dcr-1 into ~21-23 nt miRNA duplexes, with assistance from its cofactors Loqs-PA or Loqs-PB[35,39,40]. In contrast, exogenous or endogenous dsRNA precursors are processed by Dicer-2 with the help of Loqs-PD[41,42]. ATP hydrolysis by the Dicer-2's helicase domain drives the translocation of the dsRNA toward the Cap module formed by the PAZ-Platform domains of Dicer-2; upon end recognition and binding,

conformational rearrangements position the substrate near the catalytic center formed by the two RNase III domains, which cleave to generate 21-nt siRNA duplexes[43,44]. For RISC loading in *Drosophila*, miRNAs are loaded into Ago1 with Dcr-1 and its cofactors, whereas siRNAs are loaded into Ago2 with Dicer-2 and R2D2, another cofactor of Dicer-2[28,45,46].

It is generally accepted that the end thermodynamic stability of small RNA duplexes influences which strand serves as the guide during RISC assembly. In *Drosophila*, the duplex tends to have its 5′ end with lower thermodynamic stability bind to Dicer-2's Cap module, whereas its 5′ end with higher thermodynamic stability interact with R2D2. When the duplex is loaded into Ago2, the strand with the less stable 5′ terminus typically becomes the guide strand, and the opposing strand is ejected as the passenger strand[46-49]. Studies indicate that the Hsp70/Hsp90 chaperone system is essential for loading small RNAs onto Argonaute proteins: Hsp70 can first interacts with Ago2 to induce an "open" conformation, which is then maintained by Hsp90 to facilitate siRNA duplex loading mediated by the Dicer-2–R2D2 complex[7,25,50-52]. The conservation of this mechanism has been confirmed in the loading processes of *Drosophila* Ago1, mammalian Ago2, and plant AGO1, AGO4, AGO7 proteins[53-56].

Despite extensive functional and biochemical characterization, the structural mechanism of RISC loading, and in particular the architecture of the RLC, remains poorly understood, and the existence of a structurally defined RLC complex is debated. Here, we show that *Drosophila* Dicer-2–R2D2 and Ago2–Hsp90 systems can assemble into a stable protein–nucleic acid complex in the presence of siRNA duplexes. We determined the overall cryo-EM structure of the *Drosophila* RLC, which we designate as dmRLC2, and we reveal the strand-selection mechanism operative during RISC maturation within dmRLC2.

Results

In vitro identification of *Drosophila* RLC components

Full-length *Drosophila melanogaster* Ago2 (dmAgo2) consists of over 1,200 amino acids, considerably larger than other Argonaute family members[57] and is a challenge for us to isolate and purify. Structural prediction with AlphaFold suggests that the N-terminal 398 amino acids are intrinsically disordered. To facilitate production and biochemical analysis, we truncated this N-terminal segment (Δ1-398) and recombinantly overexpressed the truncated dmAgo2 in the 293F mammalian expression system[58]. Unless stated otherwise, "Ago2" refers to this truncation mutant in subsequent text. The truncated protein was purified at large scale with consistent yields and free of endogenous nucleic acid contamination.

Interestingly, mass spectrometry analysis of Ago2-containing complexes revealed co-purified endogenous Hsp90 and its co-chaperones p23 and FKBP51 (Extended Data Fig. 1)[59], indicating that an Ago2–Hsp90 system complex forms stably in cells. To characterize this assembly, we reconstituted an in vitro system consisting the purified Ago2-Hsp90 system and its substrate, the let-7 siRNA duplex, which forms a stable complex with Dicer-2–R2D2 and is subsequently transferred to Ago2[46]. This duplex contains a single nucleotide mismatch near the 5′-end on the Dicer-2-binding side, resulting in reduced thermodynamic stability at that terminus (Fig. 1a), a feature that may influence strand selection during RISC loading. We observed no evident interaction between the Ago2–Hsp90 system complex and either let-7 single stranded RNA (data not shown) or the let-7 duplex (Extended Data Fig. 2a-c), a result that contrasts with reports for human Ago2[10]. Previous studies have established that R2D2 plays a critical role in delivering siRNA duplexes during RISC assembly[60]. Building on this well-characterized function, we hypothesize that efficient loading of siRNA duplexes into Ago2 requires coordinated assistance from Dicer-2 and its cofactors.

In order to characterize the RISC-loading and maturation process, we designed fluorescently labeled target RNAs corresponding to the thermodynamically defined guide strand and passenger strand in the let-7 siRNA duplex, termed guide RNA Target

and passenger RNA Target, respectively (Fig. 1b)[46,50]. As hypothesized, we found that Ago2 can exert significant cleavage activity on the guide RNA Target only in the presence of Dicer-2–R2D2 and let-7 siRNA duplex (Fig. 1c,d), while the cleavage efficiency on the passenger RNA Target is much lower than that on the guide RNA Target (Extended Data Fig. 3). These results further supported our assignment of the guide and passenger strands, consistent with previous studies. As expected for RNase activity requirement of Ago2, Mg^{2+} is indispensable for the exertion of cleavage.

Dicer-2 is known to have at least two co-factor proteins, the R2D2 and Loqs-PD, which are also structurally similar, both harboring tandem dsRBDs with a typical αββββα topology. The two cofactors bind to distinct sites on Dicer-2's helicase domain and exhibit substantial functional differences[61]. Owing to their distinct binding sites on the Dicer-2's helicase domain, the two proteins can simultaneously associate with Dicer-2 without steric hindrance[62]. Loqs-PD not only significantly enhances the cleavage activity of Dicer-2 toward dsRNA substrates, but also facilitates the cleavage of highly structured endo-siRNA precursors by Dicer-2[43,44]. However, whether it can load the cleavage products into Ago2 remains unknown. Therefore, we examined the effect of the Dicer-2–Loqs-PD complex on the delivery of let-7 duplex to the Ago2–Hsp90 system complex by the in vitro cleavage assay. The Dicer-2–Loqs-PD complex exhibited a capability to deliver small RNA for RISC cleavage, but at an efficiency much lower than Dicer-2–R2D2 albeit slightly higher than Dicer-2 alone (Fig. 1e and Extended Data Fig. 3). In conclusion, R2D2 serves as an indispensable cofactor for the efficient transfer of siRNA duplex from Dicer-2 to Ago2.

Overall structure of the dmRLC2

The in vitro reconstituted system with full RISC loading activity includes Dicer-2–R2D2, siRNA duplex, and the Ago2–Hsp90 system. We therefore reasoned, from the other angle, that the let-7 siRNA duplex may bridge a direct interaction between the Dicer-2-R2D2 and the Ago2 to form a stable complex. Indeed, in the presence of let-7

siRNA duplex, Dicer-2–R2D2 and the Ago2–Hsp90 system complex can be pulled down together (Extended Data Fig. 2d) and, in a proper incubation condition, can form a stable peak on size-exclusion chromatography (Fig. 2a-c and Extended Data Fig. 4). The peak exhibited a distinct forward shift than the Dicer-2–R2D2–siRNA duplex complex alone or the incubation system of the Ago2–Hsp90 system with siRNA duplex, indicating the presence of a stable complex, which we designate as the dmRLC2 (Extended Data Fig. 4a). The dmRLC2 complex showed significant nucleic acid binding than the incubation system of the Ago2–Hsp90 system and siRNA duplex (Extended Data Fig. 4b) and its composition matched an appropriate stoichiometry of Dicer-2–R2D2, siRNA duplex, and the Ago2–Hsp90 system (Fig. 2c,d).

We employed cryo-EM to resolve the structure of dmRLC2. During the structure determination process, we could clearly observe that the complex consists of two lobes, with an overall calculated resolution of 4.37 Å (Extended Data Fig. 5). At this resolution, one lobe contains Dicer-2, R2D2, siRNA duplex, and partial density of Ago2, while the other lobe comprises Hsp90 dimer, two p23 molecules, FKBP51, and partial density of Ago2. There is considerable flexibility in the connection between the two lobes (Extended Data Movie 1), but each lobe itself exhibits relative rigidity. We thus performed local reconstruction of the two lobes separately and determined an average structure of dmRLC2 at a resolution of ~3 Å: the lobe with a resolution of 2.85 Å includes Dicer-2, R2D2, siRNA duplex, and the MID domain of Ago2, while the other lobe with a resolution of 2.97 Å contains Hsp90α, Hsp90β, two p23 molecules, FKBP51, and the PIWI domain of Ago2 (Extended Data Fig. 5). We finally fit the structure of the two lobes into the overall cryo-EM map and combined them to yield a high-resolution reconstruction of the dmRLC2 (Fig. 2e and Extended Data Movie 2).

Protein-nucleic acid interactions in the dmRLC2

In the resolved dmRLC2, the siRNA duplex remains stably bound to Dicer-2 with the assistance of R2D2, consistent with previous reports[46] (Extended Data Fig. 6).

However, a striking difference from previous observations is that the RNA duplex forms obvious interactions with Ago2 in dmRLC2, indicating that the RNA transfer process to Ago2 has already been initiated (Fig. 3a-c).

In this dmRLC2 structure, U21 at the 3′-end of the passenger strand in the siRNA duplex is bound within the 3′-end binding pocket formed by the PAZ domain of Dicer-2. The ribose of U21 forms hydrogen bonds with Dicer-2's I970, while the phosphodiester bond forms hydrogen bonds with Dicer-2's Y886 and Y925 respectively (Fig. 3d). In contrast, the 5′-end of the guide strand in the siRNA duplex is not bound to the 5′-end binding pocket in the Platform domain; instead, it undergoes a conformational flip and is positioned away from the Platform domain (Fig. 3c,e)[43]. U1 and G2 of guide strand extend into the binding pocket within the MID domain of Ago2, whose Y897, K901, K935, and K939 interact with the phosphate group of U1 via hydrogen bonds. Ago2's Y897 forms π–π stacking with the aromatic ring of base U1, whereas Ago2's K916 and T919 jointly interact with the phosphodiester bond between U1 and G2. The 5′-monophosphate at the very end of the guide strand is critical for stable binding to the MID domain. Additionally, Ago2's N931 forms hydrogen bonds with G2 (Fig. 3e). Such an interaction between the 5′-end of guide strand and three lysine residues and one tyrosine residue of Ago2's MID domain is highly conserved in the hAgo2-RNA complex[63] (Extended Data Fig. 7).

On the other end, the let-7 siRNA duplex has extensive interactions with the R2D2 protein. R2D2's dsRBD1, dsRBD2, and the 2Helix region within the protein's CTD form extensive hydrogen-bonding interactions with both the guide and passenger strands of the siRNA duplex's stem, spanning approximately 15 nt and thereby anchoring the siRNA duplex in proper position (Fig. 3b, f-g, and Extended Data Movie 2). The 3′-end of the guide strand binds to the 2Helix region of R2D2, orienting the RNA stem to the right direction (Fig. 3h). In the structure, we also resolved a long linker of Dicer-2 (residues 1015–1087, termed as CR-linker by us) that was invisible in previous structures (Extended Data Fig. 8). The CR-linker wraps around and spans the

Cap, Core, and Base modules of Dicer-2 and interacts extensively with the Platform, RNase IIIa (RIIIa), RIIIai, and dsRBD domains of Dicer-2, as well as the dsRBD2 domain of R2D2. This linker thereby stabilizes the overall architecture, anchors the dsRBD of Dicer-2 in a seatbelt-like manner, and shields Dicer-2's dsRBD away from the siRNA duplex, which may facilitate releasing siRNA duplex from Dicer-2 in later process.

Nascent siRNA strand selection by Ago2

Our structural analysis indicates that the siRNA terminus adjacent to Dicer-2's Cap module positions the 5′ end of the guide strand to fit within Ago2's MID domain. This arrangement suggests that the relative placement of the siRNA duplex with respect to Dicer-2, rather than differences in terminal thermodynamics, governs guide strand selection during RISC loading.

Given that dsRNA processing by Dicer-2 and siRNA delivery to Ago2 are continuous, we designed a dsRNA substrate that can be diced by Dicer-2 to yield nascent siRNA duplexes that are subsequently delivered to Ago2[64]. To minimize unintended siRNA generation by Dicer-2, the substrate was designed with a loose, open end on one terminus and a fully complementary dsRNA structure with a 2-nt 3′ overhang on the other terminus [43]. Based on prior studies, this architecture biases processing to proceed from the terminus with complementary dsRNA structure, producing the expected cleavage products. We designated this RNA as the long let-7 precursor (Fig. 4a).

Cleavage assays showed that Ago2 exhibits substantial cleavage activity only when the Dicer-2–R2D2 complex is present, and this activity is restricted to the guide RNA Target (Fig. 4b,c). Under the same conditions, Dicer-2 alone, or Dicer-2 together with its cofactors, efficiently dices the long let-7 precursor to generate nascent siRNA duplexes (Extended Data Fig. 9 and 10). Collectively, these results indicates that, in vitro, Dicer-2 can hand off 21-nt siRNA duplex products to Ago2 with either R2D2 or

Loqs-PD, but R2D2 remains essential for the entire loading pathway - from dsRNA processing to mature RISC assembly - and is especially critical for delivering nascent siRNA duplexes.

Here, both termini of the dicing products from the designed long let-7 precursor exhibit similar thermodynamic stability. However, during the dicing process, the 5′ end that binds to the binding pocket formed by the Dicer-2's PAZ-Platform domain is more critical for guide strand selection. Specifically, the strand whose 5′ end engages the Platform domain during processing is selected as the guide strand after delivery to Ago2. This preference is consistent with the lower stability and conservation of the Dicer-2's Platform 5′ binding pocket compared with the PAZ binding pocket, which facilitates dissociation of the 5′ end from the Platform domain to enable Ago2 loading.

The indispensable role of R2D2 in siRNA loading

Our results show that R2D2 enables loading of nascent siRNA duplexes into Ago2, whereas Loqs-PD does not. In the structure, the dsRBDs of R2D2 approach the siRNA duplex and form stable interactions, pulling the duplex outward and away from Dicer-2's Platform to facilitate subsequent loading into Ago2.

To dissect the distinct roles of R2D2 in RISC loading, we engineered R2D2 truncation mutants: R2D2△dsRBD1 (deletion of dsRBD1), R2D2△dsRBD2 (deletion of dsRBD2), and R2D2△2Helix (deletion of the 2Helix region in the CTD). All three deletions markedly reduced the transfer efficiency of the mature 21-nt siRNA duplex (Extended Data Fig. 9a). In the context of the long let-7 precursor, these truncations did not disrupt Dicer-2-mediated dicing to yield nascent siRNA duplexes, but they nearly abolished cleavage of both guide and passenger RNA targets (Fig. 4e, and Extended Data Fig. 9b,c). Collectively, these data suggest that the relative positioning of the dsRBDs to the RNA – rather than their absolute sequence conservation - facilitate siRNA transfer to Ago2. The dsRBDs appear to engage the siRNA stem distal to the

Dicer-2 Cap module, effectively positioning the duplex away from the Dicer-2's catalytic center.

In order to distinguish the mechanistic difference between R2D2 and Loqs-PD, we constructed two chimeric cofactor proteins: chLoqs_R2D2, combining Loqs-PD dsRBDs with the R2D2 CTD, and chR2D2_Loqs, combining R2D2 dsRBDs with the Loqs-PD CTD (Fig. 4d). In vitro cleavage assays revealed that chLoqs_R2D2 markedly enhances cleavage of the guide RNA Target compared with chR2D2_Loqs and wild-type Loqs-PD, regardless of whether the 21-nt Dicer-2 product or the nascent siRNA-duplex-generating substrate is present. Conversely, none of the constructs produced clear cleavage of the passenger RNA Target (Fig. 4f and Extended Data Fig. 10a,b). Importantly, chLoqs_R2D2 did not substantially alter Dicer-2's dicing activity, a property that distinguishes Loqs-PD but aligns with R2D2-like behavior (Extended Data Fig. 9c).

Taken together, our data show that the spatial arrangement of R2D2's two dsRBDs is essential for the handoff of the bound siRNA duplex to Ago2, underscoring a nonredundant role for dsRBD positioning in RISC loading.

Interaction between the RIIIai domain of Dicer-2 and the MID domain of Ago2

The dmRLC2 structure revealed important protein-protein interactions between Dicer-2 and Ago2. In additional to engaging the substrate RNA, Ago2's MID domain establishes a robust interaction with the Dicer-2 RIIIai domain (Extended Data Movie 2). The interface buries approximately 1,410 Å^2 at a 2 Å probe radius, and is dominated by electrostatic interactions (Fig. 5a-d). Moreover, a network of hydrogen bonds - Y823 and Y834 in the Ago2 MID domain with Y1343 and E1351 in the Dicer-2 RIIIai domain, respectively – contribute to a tightly constrained relative positioning (Fig. 5e). This dual mode of interaction likely reinforces the coordinated alignment of Ago2 and Dicer-2 during loading.

Notably, the RIIIai domain does not undergo positional or conformational changes upon siRNA duplex binding (comparison data not shown)[44]. However, in the absence of siRNA duplex, Ago2 fails to interact with Dicer-2 (Extended Data Fig. 2). To assess the role of the RIIIai domain during transfer, we constructed a truncation mutant, Dicer-2ΔRIIIai, deleting the RIIIai domain. When supplied with 21-nt siRNA duplex, target RNA cleavage efficiency was significantly reduced with Dicer-2ΔRIIIai compared with wild-type (Extended Data Fig. 11a). With the long let-7 precursor, almost no cleavage activity was observed for Dicer-2ΔRIIIai (Extended Data Fig. 11b). We propose that the RIIIai domain provides a platform for the MID domain of Ago2, enabling stable substrate RNA association. The interaction between RIIIai and MID is not rigid or constitutive, explaining the lack of stable binding in the absence of small RNA substrates, and offering a structural basis for the MID Dicer-2 dissociation after RNA transfer.

Extended conformation of Ago2 in the Hsp90 system

Our dmRLC2 structure reveals an unexpected involvement of the Hsp90 system and a pronounced conformational rearrangement of Ago2 compared with prior structures. In the resolved model, Ago2 physically links the Dicer-2 module to the Hsp90 system via Ago2's MID and PIWI domains (Fig. 2e and Extended Data Movie 2). The cryo-EM density indicates that the MID domain sits markedly farther from the PIWI domain than in the canonical, substrate-loaded Ago2 architecture (PDB: 4W5N)[63] (Extended Data Fig. 12a,b). Quantitatively, the centroid-centroid distance between the MID and PIWI domains is 49.3 Å in our dmRLC2 structure, versus 32.1 Å in human Ago2 (Fig. 5a,f), underscoring a substantial, functionally relevant rearrangement. This rearrangement may reflect a distinct loading or regulatory state facilitated by the Hsp90 system.

While the Ago2 MID domain predominantly engages the Dicer-2 RIIIai domain, the PIWI domain establishes extensive electrostatic interactions and hydrogen bonds

with multiple Hsp90 components, including Hsp90α and Hsp90β (Fig. 5a,f). Specific contacts include Hsp90α's I280 and R346 hydrogen-bonding with PIWI's E1089 and E1023, respectively (Fig. 5g,h), and Hsp90β's Y627 forming a hydrogen bond with PIWI's I1013 (Fig. 5i). The buried interface areas at a 2 Å probe are 565 Å^2 (Hsp90α-PIWI) and 720 Å^2 (Hsp90β-PIWI) respectively (Extended Data Fig. 13).

Concomitantly, we observed that a linker within the Ago2 L2 traverses the cleft formed in the closed Hsp90α-Hsp90β dimer (Fig. 5j). Although densities for Ago2 NTD and PAZ domains were not resolved, this arrangement partitions Ago2 into two segments: a Dicer-proximal segment containing the MID and PIWI domains, and an distal segment comprising the NTD and PAZ domains on the opposite side of the Hsp90 dimer (Fig. 5a,f). In addition to interacting with Hsp90, the L2 region forms tight contacts with the adjacent PIWI domain via β-sheet stacking (Fig. 5j,k). Specifically, residues N772, I775, and V777 in L2 hydrogen-bond with Q996, M995, and Y993 in PIWI, respectively (Fig. 5k). We propose that these L2-PIWI contacts provide a structural basis for the stable Ago2-Hsp90 association. Although Ago2 adopts an overall extended conformation at this stage, domain-level conservation remains high (Extended Data Fig. 7 and 12c,d).

Together, these interactions stabilize a defined orientation between the Ago2 domains and the Hsp90 machinery, constraining the otherwise flexible Ago2 domains and promoting efficient siRNA duplex transfer. This provides robust structural support for the previously proposed model in which the Hsp90 chaperone maintains Ago2 in an open conformation[50]. Furthermore, this defined positional relationship explains why cryo-EM density is observed for the 5′ end of the guide strand bound in the MID domain of Ago2, whereas no corresponding density is seen for the PAZ domain, which contains the 3′-end binding pocket. Our structural data also clearly explain why we failed to observe a stable complex between Ago2, Hsp90, and the siRNA duplex in our in vitro assays. We propose that complete loading of the siRNA duplex into Ago2 is accompanied by the disassembly of the Hsp90 machinery. This model is further

supported by the structure of the dmRLC2 complex, which demonstrates that Hsp90 is indispensable for stabilizing the relatively flexible open state of Ago2 under physiological conditions.

Discussion

As a core mechanism of gene regulation, the RNAi pathway is not only fundamental to biology but also holds significant promise for the development of precision medicines. Despite decades of research since the initial discovery of the RNAi phenomenon, the complete molecular mechanisms of the pathway remain elusive. In particular, the RISC-loading process—specifically how the processing of precursor RNAs by Dicer is coupled with the loading of the resulting small RNA into an Argonaute protein—is largely unknown.

In this study, we reconstituted the dmRLC2 of the *Drosophila* Dicer-2-mediated siRNA pathway in vitro and determined its high-resolution structure, thereby filling a critical gap in our understanding of the pathway from small RNA maturation to RISC assembly. This structural information reveals the molecular basis of siRNA handover from Dicer-2 to Ago2 and the mechanism of guide strand selection, in which all protein components act in a concerted and indispensable manner (Extended Data Movie 2). Our findings not only demonstrate that the RISC-loading complex can be stably assembled, but also reveal that the siRNA guide strand originates from a defined source: the strand of the duplex whose 5′ end preferentially engages the Dicer-2 Platform domain. This processing occurs through continuous ATP hydrolysis by Dicer-2, and the cleavage products are directly loaded into Ago2 to form RISC in a sequential and deterministic manner (Fig. 6).

Strand selection in the dmRLC2 pathway does not necessarily depend on the thermodynamic stability of the siRNA duplex ends, a clear distinction from the miRNA loading process. In miRNA loading, either the 5′ strand or 3′ strand of a miRNA duplex can be selected as the guide strand after Dicer-mediated processing, as revealed by miRNA sequencing data and the miRBase database[65]. The siRNA loading model

reported here therefore cannot fully account for the miRNA loading process, which likely involves more complex regulatory mechanisms. This difference may be explained by the distinct biological functions of these pathways. The *Drosophila* Dicer-2-mediated siRNA pathway primarily acts as an innate immune defense against viral invasion[44]. To rapidly suppress viral replication, cells must efficiently convert viral RNA into functional RISC, and this demand for speed may bypass more nuanced strand selection mechanisms. The molecular basis for this difference likely lies in the specific cofactor proteins involved. In *Drosophila*, Dicer-2 functions in the siRNA pathway with the assistance of Loqs-PD and R2D2, whereas Dicer-1 is primarily responsible for miRNA processing with the assistance of Loqs-PA and Loqs-PB. In humans, a single Dicer protein orchestrates both pathways with the assistance of the cofactor TRBP[66]. Whether the RISC-loading mechanisms mediated by human Dicer–TRBP and *Drosophila* Dicer-1–Loqs-PA/Loqs-PB are conserved—and how they compare to the siRNA mechanism reported here—are important questions that warrant further investigation.

The Hsp90 system has been reported to function in RISC loading, but our work now reveals it to be a major structural component of the RISC-loading complex. Although we expressed and purified *Drosophila* Ago2 in mammalian cells—where it assembled with the human Hsp90 system—this hybrid complex faithfully recapitulates the small RNA loading process of Ago2. This conclusion is supported by two key observations: first, the functional mechanisms of the Hsp90 system are highly conserved across higher eukaryotes; second, the amino acid residues of Ago2 that directly interact with the Hsp90 system are nearly identical to those in its human ortholog (Extended Data Fig. 14). In contrast, FKBP51 exhibits substantially lower sequence conservation than Hsp90, suggesting that it may play a more species-specific or accessory role. We therefore conclude that Hsp90 is the primary regulator responsible for maintaining the open conformation of Ago proteins, a role that is fully supported by our structural data.

In the structure of dmRLC2, the four canonical domains of Ago2 no longer adopt the characteristic four-leaf clover arrangement. Instead, the Hsp90 system extensively reconfigures these domains and disrupts their interdomain contacts. This conformational rearrangement not only releases any pre-bound siRNA from Ago2 but also creates an environment conducive to the binding of nascent siRNA duplexes (Fig. 6). Within the complex, Hsp90 segregates Ago2 into two structural modules, thereby preventing the 3′ end of the siRNA from engaging the PAZ domain of Ago2. We therefore propose that the Hsp90 system dissociates from Ago2 during RISC maturation (Fig. 6). Although Hsp90 contains an ATP-binding site, ATP hydrolysis was reported unnecessary for the loading of siRNA into Ago2 and subsequent RISC assembly[67]. Further investigation will be necessary to dissect the downstream events following RISC assembly.

Complexes involved in RISC loading have been long-sought structural targets. The structure presented here captures but one static snapshot of a highly dynamic and complicated process. Now that we have successfully reconstituted the complex with its core components identified, future investigations can focus on the conformational dynamics and regulatory mechanisms that govern RISC loading, paving the way toward a complete molecular understanding of this fundamental pathway.

Methods

Protein expression and purification

Drosophila melanogaster Ago2 (Δ1–398) was cloned into the pCAG vector. The Ago2 plasmid was transfected into HEK293F cells cultured at 37 °C under 5% CO_2, at a cell density of 2 × 10^6 cells/mL. Cells expressing the target protein were harvested after 48 h of incubation, and the protein was purified via a 3×Flag tag (Sigma) in buffer A (50 mM HEPES pH 7.4, 150 mM NaCl, 10% glycerol), followed by size-exclusion chromatography using a Superdex 200 3.2/300 Increase column (Cytiva) equilibrated in buffer B (50 mM HEPES pH 7.4, 150 mM NaCl).

Drosophila melanogaster Dicer-2, the Dicer-2 mutant (Dicer-2ΔRIIIai), and R2D2 were cloned into the pFastBac vector. Dicer-2 and R2D2 were co-expressed in Sf9 cells using the Bac-to-Bac baculovirus expression system at 27 °C, at a cell density of 2 × 10^6 cells/mL. Cells expressing the target protein were harvested after 60 h of incubation, and the protein was purified via a 6×His tag (GenScript) in buffer C (50 mM Tris-HCl pH 8.0, 150 mM NaCl, 10% glycerol), followed by size-exclusion chromatography using a Superdex 200 3.2/300 Increase column (Cytiva) equilibrated in buffer D (50 mM Tris-HCl pH 8.0, 150 mM NaCl).

Loqs-PD and its mutants (chLoqs_R2D2, chR2D2_Loqs, R2D2ΔdsRBD1, R2D2ΔdsRBD2, and R2D2Δ2Helix) were cloned into the pET28a vector and individually expressed in *E. coli* upon IPTG induction. Proteins were first purified via a 6×His tag (GenScript). The 6×His tag was then removed by TEV protease cleavage overnight, and the sample was passed through Ni-NTA affinity chromatography again. Further purification was performed using a Superdex 200 10/300 Increase column (Cytiva) equilibrated in buffer C.

Dicer-2 and its cofactor Loqs-PD or the corresponding mutants were mixed at a 1:1.5 molar ratio, incubated on ice for 1 h, and further purified using a Superdex 200 10/300 Increase column (Cytiva) equilibrated in buffer D.

All purified proteins were snap-frozen in liquid nitrogen and stored at −80 °C until use.

In vitro cleavage assays

First, 0.35 μM Dicer-2–R2D2 complex was mixed with 0.9 μM let-7 duplex or long let-7 precursor in buffer E (30 mM HEPES-KOH pH 7.4, 100 mM KOAc, 5 mM ATP, 2 mM $Mg(OAc)_2$), and the mixture was incubated on ice for 10 min. SUPERase·In™ RNase inhibitor (Thermo Fisher Scientific) was added to the reaction system to prevent RNA degradation. Next, 0.35 μM Ago2–Hsp90 system complex was added, and the incubation was continued on ice for an additional 10 min. Subsequently, 0.04 μM 5′-FAM-labeled target RNA was added to initiate the cleavage reaction, which was then incubated at 30 °C for 2 h. Reactions were terminated by adding an equal volume of 2× formamide loading buffer. Samples were resolved by 15% denaturing urea-PAGE and visualized using a ChemiDoc MP imaging system (Bio-Rad).

Pulldown assay

Purified Ago2–Hsp90 system complex was incubated with Flag affinity beads (Sigma) in buffer F (30 mM HEPES-KOH pH 7.4, 100 mM KOAc, 2 mM $Mg(OAc)_2$) with gentle rotation at 4 °C for 1 h to immobilize the complex onto the beads. After incubation, the supernatant was removed carefully, and the beads were washed three times with 200 μL of buffer F to remove unbound proteins. Subsequently, the beads were mixed with Dicer-2–R2D2 in the presence or absence of siRNA duplex, followed by incubation with gentle rotation at 4 °C for 1 h. The supernatant was then transferred to a new microfuge tube. The beads were resuspended and washed three more times to remove non-specifically bound proteins. The beads and supernatants were mixed with 5× SDS-PAGE loading buffer and heated at 95 °C for 10 min to denature proteins. Finally, samples were analyzed by SDS-PAGE.

dmRLC2 assembly in vitro

Dicer-2–R2D2, the Ago2–Hsp90 system, and the siRNA duplex were mixed at a 1:1:1.5 molar ratio in buffer F and incubated on ice for 1 h to assemble the complex. The mixture was then loaded onto a Superdex 200 10/300 Increase column (Cytiva) pre-equilibrated with buffer F. The collected target fractions were mixed with 5× SDS-PAGE loading buffer, heated at 95 °C for 10 min to denature proteins, and analyzed by SDS-PAGE to verify complex formation.

Cryo-EM sample preparation and data collection

Cryo-EM samples were prepared using an FEI Vitrobot Mark IV at 8 °C and 100% humidity. Briefly, 4 μL of the assembled complex was applied to a Quantifoil Au 1.2/1.3 300-mesh grid, which had been glow-discharged at medium power for 30 s following 2 min of evacuation. After incubation for 1 min, the grid was blotted for 1.5 s with filter paper and immediately plunge-frozen in liquid ethane cooled by liquid nitrogen. Cryo-EM data were collected on a 300 kV Titan Krios electron microscope equipped with a Falcon 4 direct electron detector. Movies were automatically recorded in counting mode using EPU software, with defocus values ranging from −1.5 μm to −2.0 μm.

Image processing and 3D reconstruction

Raw dose-fractionated image stacks were processed using MotionCor2 for twofold Fourier binning, frame alignment, dose weighting, and frame summation. Contrast transfer function (CTF) parameters were estimated using CTFFIND4 within CryoSPARC[68-70]. Initial particles were automatically picked from high-quality micrographs using a blob picker. After several rounds of reference-free 2D classification to select high-quality particles, the selected particles were imported into RELION for multiple rounds of 3D classification [71]. Particles corresponding to the best

3D classes were subjected to high-resolution homogeneous refinement in CryoSPARC[68].

Model building and refinement

The cryo-EM map presented in this study is of sufficient quality for atomic model building. For lower-resolution regions, such as FKBP51, the model was built based on AlphaFold predictions. All models were further manually adjusted and optimized in ISOLDE (ChimeraX) and COOT[72,73]. Finally, the models were subjected to real-space refinement against the cryo-EM map in PHENIX, with secondary structure and geometry restraints applied[74]. The quality of the final refined models was validated using the PHENIX software suite, and the refinement statistics are summarized in Extended Data Table 1.

Data availability

The atomic coordinates and structure factors have been deposited in the RCSB Protein Data Bank (PDB) and Electron Microscopy Data Bank (EMDB). The PDB and EMDB codes are listed in Extended Data Table 1. For gel source images, see Supplementary Data. All other data or materials can be obtained from the corresponding author upon request. Source data are provided with this paper.

References

1 Agrawal, N. *et al.* RNA interference: biology, mechanism, and applications. *Microbiol Mol Biol Rev* **67**, 657-685 (2003). https://doi.org/10.1128/MMBR.67.4.657-685.2003

2 Elbashir, S. M., Lendeckel, W. & Tuschl, T. RNA interference is mediated by 21- and 22-nucleotide RNAs. *Genes Dev* **15**, 188-200 (2001). https://doi.org/10.1101/gad.862301

3 Fire, A. RNA-triggered gene silencing. *Trends Genet* **15**, 358-363 (1999). https://doi.org/10.1016/s0168-9525(99)01818-1

4 Shrivastava, N. & Srivastava, A. RNA interference: an emerging generation of biologicals. *Biotechnol J* **3**, 339-353 (2008). https://doi.org/10.1002/biot.200700215

5 Sioud, M. RNA Interference: Story and Mechanisms. *Methods Mol Biol* **2282**, 1-15 (2021). https://doi.org/10.1007/978-1-0716-1298-9_1

6 Tuschl, T. RNA interference and small interfering RNAs. *Chembiochem* **2**, 239-245 (2001). https://doi.org/10.1002/1439-7633(20010401)2:4<239::AID-CBIC239>3.0.CO;2-R

7 Kobayashi, H. & Tomari, Y. RISC assembly: Coordination between small RNAs and Argonaute proteins. *Biochim Biophys Acta* **1859**, 71-81 (2016). https://doi.org/10.1016/j.bbagrm.2015.08.007

8 Peters, L. & Meister, G. Argonaute proteins: mediators of RNA silencing. *Mol Cell* **26**, 611-623 (2007). https://doi.org/10.1016/j.molcel.2007.05.001

9 Iwakawa, H. O. & Tomari, Y. Life of RISC: Formation, action, and degradation of RNA-induced silencing complex. *Mol Cell* **82**, 30-43 (2022). https://doi.org/10.1016/j.molcel.2021.11.026

10 Schirle, N. T. & MacRae, I. J. The crystal structure of human Argonaute2. *Science* **336**, 1037-1040 (2012). https://doi.org/10.1126/science.1221551

11 Elkayam, E. *et al.* The structure of human argonaute-2 in complex with miR-20a. *Cell* **150**, 100-110 (2012). https://doi.org/10.1016/j.cell.2012.05.017

12 Wang, Y. *et al.* Structure of an argonaute silencing complex with a seed-containing guide DNA and target RNA duplex. *Nature* **456**, 921-926 (2008). https://doi.org/10.1038/nature07666

13 Czech, B. *et al.* An endogenous small interfering RNA pathway in Drosophila. *Nature* **453**, 798-802 (2008). https://doi.org/10.1038/nature07007

14 Cooper, A. M., Silver, K., Zhang, J., Park, Y. & Zhu, K. Y. Molecular mechanisms influencing efficiency of RNA interference in insects. *Pest Manag Sci* **75**, 18-28 (2019). https://doi.org/10.1002/ps.5126

15 Zhu, K. Y. & Palli, S. R. Mechanisms, Applications, and Challenges of Insect RNA Interference. *Annu Rev Entomol* **65**, 293-311 (2020). https://doi.org/10.1146/annurev-ento-011019-025224

16 Li, C. & Zamore, P. D. RNA Interference and Small RNA Analysis. *Cold Spring Harb Protoc* **2019** (2019). https://doi.org/10.1101/pdb.top097436

17 Tomari, Y. & Zamore, P. D. Perspective: machines for RNAi. *Genes Dev* **19**, 517-529 (2005). https://doi.org/10.1101/gad.1284105

18 Wu, J., Yang, J., Cho, W. C. & Zheng, Y. Argonaute proteins: Structural features, functions and emerging roles. *J Adv Res* **24**, 317-324 (2020). https://doi.org/10.1016/j.jare.2020.04.017

19 Gagnon, K. T. Loading of Argonaute Protein with Small Duplex RNA in Cellular Extracts. *Methods Mol Biol* **1421**, 53-67 (2016). https://doi.org/10.1007/978-1-4939-3591-8_6

20 Liu, Z. *et al.* Cryo-EM Structure of Human Dicer and Its Complexes with a Pre-miRNA Substrate. *Cell* **173**, 1191-1203 e1112 (2018). https://doi.org/10.1016/j.cell.2018.03.080

21 Taylor, D. W. *et al.* Substrate-specific structural rearrangements of human Dicer. *Nat Struct Mol Biol* **20**, 662-670 (2013). https://doi.org/10.1038/nsmb.2564

22 Kim, K., Lee, Y. S., Harris, D., Nakahara, K. & Carthew, R. W. The RNAi pathway initiated by Dicer-2 in Drosophila. *Cold Spring Harb Symp Quant Biol* **71**, 39-44 (2006). https://doi.org/10.1101/sqb.2006.71.008

23 Sabin, L. R. *et al.* Dicer-2 processes diverse viral RNA species. *PLoS One* **8**, e55458 (2013). https://doi.org/10.1371/journal.pone.0055458

24 Torrez, R. M., Ohi, M. D. & Garner, A. L. Structural Insights into the Advances and Mechanistic Understanding of Human Dicer. *Biochemistry* **62**, 1-16 (2023). https://doi.org/10.1021/acs.biochem.2c00570

25 Iwasaki, S. *et al.* Defining fundamental steps in the assembly of the Drosophila RNAi enzyme complex. *Nature* **521**, 533-536 (2015). https://doi.org/10.1038/nature14254

26 Miyoshi, T., Takeuchi, A., Siomi, H. & Siomi, M. C. A direct role for Hsp90 in pre-RISC formation in Drosophila. *Nat Struct Mol Biol* **17**, 1024-1026 (2010). https://doi.org/10.1038/nsmb.1875

27 Matranga, C., Tomari, Y., Shin, C., Bartel, D. P. & Zamore, P. D. Passenger-strand cleavage facilitates assembly of siRNA into Ago2-containing RNAi enzyme complexes. *Cell* **123**, 607-620 (2005). https://doi.org/10.1016/j.cell.2005.08.044

28 Miyoshi, K., Okada, T. N., Siomi, H. & Siomi, M. C. Characterization of the miRNA-RISC loading complex and miRNA-RISC formed in the Drosophila miRNA pathway. *RNA* **15**, 1282-1291 (2009). https://doi.org/10.1261/rna.1541209

29 Tomari, Y. *et al.* RISC assembly defects in the Drosophila RNAi mutant armitage. *Cell* **116**, 831-841 (2004). https://doi.org/10.1016/s0092-8674(04)00218-1

30 Gregory, R. I., Chendrimada, T. P., Cooch, N. & Shiekhattar, R. Human RISC couples microRNA biogenesis and posttranscriptional gene silencing. *Cell* **123**, 631-640 (2005). https://doi.org/10.1016/j.cell.2005.10.022

31 Wang, H. W. *et al.* Structural insights into RNA processing by the human RISC-loading complex. *Nat Struct Mol Biol* **16**, 1148-1153 (2009). https://doi.org/10.1038/nsmb.1673

32 MacRae, I. J., Ma, E., Zhou, M., Robinson, C. V. & Doudna, J. A. In vitro reconstitution of the human RISC-loading complex. *Proc Natl Acad Sci U S A* **105**, 512-517 (2008). https://doi.org/10.1073/pnas.0710869105

33 Okamura, K., Ishizuka, A., Siomi, H. & Siomi, M. C. Distinct roles for Argonaute proteins in small RNA-directed RNA cleavage pathways. *Genes Dev* **18**, 1655-1666 (2004). https://doi.org/10.1101/gad.1210204

34 Ameres, S. L., Hung, J. H., Xu, J., Weng, Z. & Zamore, P. D. Target RNA-directed tailing and trimming purifies the sorting of endo-siRNAs between the two Drosophila Argonaute proteins. *RNA* **17**, 54-63 (2011). https://doi.org/10.1261/rna.2498411

35 Jouravleva, K. *et al.* Structural basis of microRNA biogenesis by Dicer-1 and its partner protein Loqs-PB. *Mol Cell* **82**, 4049-4063 e4046 (2022). https://doi.org/10.1016/j.molcel.2022.09.002

36 Wei, X., Li, J. & Li, Y. RNA interfering machinery: new insight into the Dicer-2 complexes in the dsRNA-processing cycle. *Signal Transduct Target Ther* **8**, 2 (2023). https://doi.org/10.1038/s41392-022-01272-9

37 Jin, W., Wang, J., Liu, C. P., Wang, H. W. & Xu, R. M. Structural Basis for pri-miRNA Recognition by Drosha. *Mol Cell* **78**, 423-433 e425 (2020). https://doi.org/10.1016/j.molcel.2020.02.024

38 Partin, A. C. *et al.* Cryo-EM Structures of Human Drosha and DGCR8 in Complex with Primary MicroRNA. *Mol Cell* **78**, 411-422 e414 (2020). https://doi.org/10.1016/j.molcel.2020.02.016

39 Tsutsumi, A., Kawamata, T., Izumi, N., Seitz, H. & Tomari, Y. Recognition of the pre-miRNA structure by Drosophila Dicer-1. *Nat Struct Mol Biol* **18**, 1153-1158 (2011). https://doi.org/10.1038/nsmb.2125

40 Jakob, L. *et al.* Structural and functional insights into the fly microRNA biogenesis factor Loquacious. *RNA* **22**, 383-396 (2016). https://doi.org/10.1261/rna.055426.115

41 Trettin, K. D., Sinha, N. K., Eckert, D. M., Apple, S. E. & Bass, B. L. Loquacious-PD facilitates Drosophila Dicer-2 cleavage through interactions with the helicase domain and dsRNA. *Proc Natl Acad Sci U S A* **114**, E7939-E7948 (2017). https://doi.org/10.1073/pnas.1707063114

42 Jonely, M., Singh, R. K., Donelick, H. M., Bass, B. L. & Noriega, R. Loquacious-PD regulates the terminus-dependent molecular recognition of Dicer-2 toward double-stranded RNA. *Chem Commun (Camb)* **57**, 10879-10882 (2021). https://doi.org/10.1039/d1cc03843e

43 Cao, N. *et al.* Structural basis of endo-siRNA processing by Drosophila Dicer-2 and Loqs-PD. *Nucleic Acids Res* **53** (2025). https://doi.org/10.1093/nar/gkaf102

44 Su, S. *et al.* Structural insights into dsRNA processing by Drosophila Dicer-2-Loqs-PD. *Nature* **607**, 399-406 (2022). https://doi.org/10.1038/s41586-022-04911-x

45 Yang, J. S. *et al.* Intertwined pathways for Argonaute-mediated microRNA biogenesis in Drosophila. *Nucleic Acids Res* **42**, 1987-2002 (2014). https://doi.org/10.1093/nar/gkt1038

46 Yamaguchi, S. *et al.* Structure of the Dicer-2-R2D2 heterodimer bound to a small RNA duplex. *Nature* **607**, 393-398 (2022). https://doi.org/10.1038/s41586-022-04790-2

47 Tomari, Y., Matranga, C., Haley, B., Martinez, N. & Zamore, P. D. A protein sensor for siRNA asymmetry. *Science* **306**, 1377-1380 (2004). https://doi.org/10.1126/science.1102755

668 48 Khvorova, A., Reynolds, A. & Jayasena, S. D. Functional siRNAs and miRNAs
669 exhibit strand bias. *Cell* **115**, 209-216 (2003). https://doi.org/10.1016/s0092-
670 8674(03)00801-8
671 49 Schwarz, D. S. *et al.* Asymmetry in the assembly of the RNAi enzyme complex.
672 *Cell* **115**, 199-208 (2003). https://doi.org/10.1016/s0092-8674(03)00759-1
673 50 Tsuboyama, K., Tadakuma, H. & Tomari, Y. Conformational Activation of
674 Argonaute by Distinct yet Coordinated Actions of the Hsp70 and Hsp90
675 Chaperone Systems. *Mol Cell* **70**, 722-729 e724 (2018).
676 https://doi.org/10.1016/j.molcel.2018.04.010
677 51 Nakanishi, K. Anatomy of RISC: how do small RNAs and chaperones activate
678 Argonaute proteins? *Wiley Interdiscip Rev RNA* **7**, 637-660 (2016).
679 https://doi.org/10.1002/wrna.1356
680 52 Naruse, K., Matsuura-Suzuki, E., Watanabe, M., Iwasaki, S. & Tomari, Y. In
681 vitro reconstitution of chaperone-mediated human RISC assembly. *RNA* **24**, 6-
682 11 (2018). https://doi.org/10.1261/rna.063891.117
683 53 Endo, Y., Iwakawa, H. O. & Tomari, Y. Arabidopsis ARGONAUTE7 selects
684 miR390 through multiple checkpoints during RISC assembly. *EMBO Rep* **14**,
685 652-658 (2013). https://doi.org/10.1038/embor.2013.73
686 54 Iwasaki, S. *et al.* Hsc70/Hsp90 chaperone machinery mediates ATP-dependent
687 RISC loading of small RNA duplexes. *Mol Cell* **39**, 292-299 (2010).
688 https://doi.org/10.1016/j.molcel.2010.05.015
689 55 Johnston, M., Geoffroy, M. C., Sobala, A., Hay, R. & Hutvagner, G. HSP90
690 protein stabilizes unloaded argonaute complexes and microscopic P-bodies in
691 human cells. *Mol Biol Cell* **21**, 1462-1469 (2010).
692 https://doi.org/10.1091/mbc.e09-10-0885
693 56 Ye, R. *et al.* Cytoplasmic assembly and selective nuclear import of Arabidopsis
694 Argonaute4/siRNA complexes. *Mol Cell* **46**, 859-870 (2012).
695 https://doi.org/10.1016/j.molcel.2012.04.013

57 Narita, H., Shima, T., Iizuka, R. & Uemura, S. N-terminal region of Drosophila melanogaster Argonaute2 forms amyloid-like aggregates. *BMC Biol* **21**, 78 (2023). https://doi.org/10.1186/s12915-023-01569-3

58 Liu, Y. *et al.* C3PO, an endoribonuclease that promotes RNAi by facilitating RISC activation. *Science* **325**, 750-753 (2009). https://doi.org/10.1126/science.1176325

59 Tian, X. *et al.* Molecular mechanism of PINK1 regulation by the Hsp90 machinery. *Nat Commun* **16**, 10801 (2025). https://doi.org/10.1038/s41467-025-65859-w

60 Liu, X., Jiang, F., Kalidas, S., Smith, D. & Liu, Q. Dicer-2 and R2D2 coordinately bind siRNA to promote assembly of the siRISC complexes. *RNA* **12**, 1514-1520 (2006). https://doi.org/10.1261/rna.101606

61 Marques, J. T. *et al.* Loqs and R2D2 act sequentially in the siRNA pathway in Drosophila. *Nat Struct Mol Biol* **17**, 24-30 (2010). https://doi.org/10.1038/nsmb.1735

62 Deng, T. *et al.* Structural mechanism of R2D2 and Loqs-PD synergistic modulation on DmDcr-2 oligomers. *Nat Commun* **14**, 5228 (2023). https://doi.org/10.1038/s41467-023-40919-1

63 Schirle, N. T., Sheu-Gruttadauria, J. & MacRae, I. J. Structural basis for microRNA targeting. *Science* **346**, 608-613 (2014). https://doi.org/10.1126/science.1258040

64 Donelick, H. M. *et al.* In vitro studies provide insight into effects of Dicer-2 helicase mutations in Drosophila melanogaster. *RNA* **26**, 1847-1861 (2020). https://doi.org/10.1261/rna.077289.120

65 Kozomara, A., Birgaoanu, M. & Griffiths-Jones, S. miRBase: from microRNA sequences to function. *Nucleic Acids Res* **47**, D155-D162 (2019). https://doi.org/10.1093/nar/gky1141

66 Chendrimada, T. P. *et al.* TRBP recruits the Dicer complex to Ago2 for microRNA processing and gene silencing. *Nature* **436**, 740-744 (2005). https://doi.org/10.1038/nature03868

67 Noddings, C. M., Wang, R. Y., Johnson, J. L. & Agard, D. A. Structure of Hsp90-p23-GR reveals the Hsp90 client-remodelling mechanism. *Nature* **601**, 465-469 (2022). https://doi.org/10.1038/s41586-021-04236-1

68 Punjani, A., Rubinstein, J. L., Fleet, D. J. & Brubaker, M. A. cryoSPARC: algorithms for rapid unsupervised cryo-EM structure determination. *Nat Methods* **14**, 290-296 (2017). https://doi.org/10.1038/nmeth.4169

69 Zheng, S. Q. *et al.* MotionCor2: anisotropic correction of beam-induced motion for improved cryo-electron microscopy. *Nat Methods* **14**, 331-332 (2017). https://doi.org/10.1038/nmeth.4193

70 Rohou, A. & Grigorieff, N. CTFFIND4: Fast and accurate defocus estimation from electron micrographs. *J Struct Biol* **192**, 216-221 (2015). https://doi.org/10.1016/j.jsb.2015.08.008

71 Zivanov, J. *et al.* New tools for automated high-resolution cryo-EM structure determination in RELION-3. *Elife* **7** (2018). https://doi.org/10.7554/eLife.42166

72 Emsley, P. & Cowtan, K. Coot: model-building tools for molecular graphics. *Acta Crystallogr D Biol Crystallogr* **60**, 2126-2132 (2004). https://doi.org/10.1107/S0907444904019158

73 Goddard, T. D. *et al.* UCSF ChimeraX: Meeting modern challenges in visualization and analysis. *Protein Sci* **27**, 14-25 (2018). https://doi.org/10.1002/pro.3235

74 Adams, P. D. *et al.* PHENIX: a comprehensive Python-based system for macromolecular structure solution. *Acta Crystallogr D Biol Crystallogr* **66**, 213-221 (2010). https://doi.org/10.1107/S0907444909052925

Acknowledgments

We thank Jianlin Lei, Fan Yang and Xiaomin Li at Tsinghua University for assistance with cryo-EM sample screening. We acknowledge the Tsinghua University Branch of the China National Center for Protein Sciences (Beijing) and Shuimu BioSciences Ltd. for providing the cryo-EM facility support and the computational facility support.

Funding

This research is supported by the National Natural Science Foundation of China (32130054 to H.-W. W. and J.W.; 22227807 to J.W.)., National Key Research and Development Program of China (2024YFA1307301 to H.-W. W.), and Major Project of Guangzhou National Laboratory (GZNL2024A03004 to H.-W. W.)

Author contributions

H.-W. W. and J.W. conceived the study. N.C., J.W., and H.-W. W. designed experiments. N.C. and J.W. prepared the samples and performed the biochemical experiments and analyzed the data. N.C. and J.W. performed cryo-EM experiments, structure determination and built the models. N.C., J.W. and H.-W. W. analyzed data, N.C., J.W. and H.-W. W. wrote the manuscript.

Confliction of interest

The authors declare no confliction of interest.

Data deposition

The cryo-EM density map of dmRLC2 and the corresponding atomic model presented in this study have been deposited in the wwPDB OneDep system under the accession codes EMD-69434 (EMDB) and 24BO (PDB), respectively. The accession codes for the related focused-refinement maps (used to reconstruct the composite map)

780 and the low-resolution consensus map are EMD-69587, EMD-69588, and EMD-69589,
781 respectively.
782

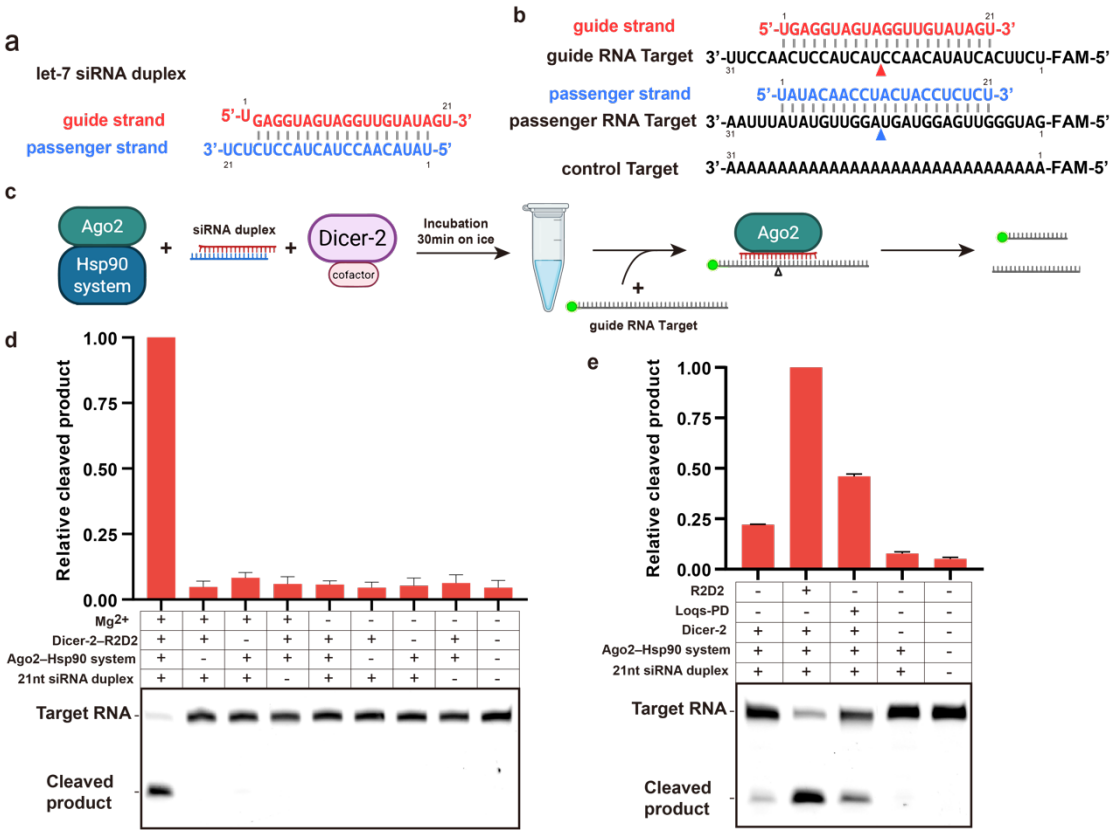

Fig. 1| Composition and functional characterization of RISC loading complex. a, Nucleotide sequences of the let-7 siRNA duplex, comprising both guide and passenger strands. **b**, Nucleotide sequences of FAM-labeled target RNAs complementary to each strand of the let-7 siRNA duplex. The target RNA complementary to the guide strand is denoted as the guide RNA Target, while that complementary to the passenger strand is termed the passenger RNA Target. A control Target lacking complementarity to either strand is also included. The red and blue triangles indicate the Ago2 cleavage sites directed by the guide strand and passenger strand, respectively. **c**, Schematic representation of the cleavage assay workflow. **d**, Cleavage assays of the Ago2–Hsp90 system using a FAM-labeled guide RNA Target. Reactions were carried out in cleavage assay buffer at 30 °C, with or without Dicer-2–R2D2, 21 nt siRNA duplex, or Mg^{2+} (bottom panel). Cleavage efficiencies are quantified in the top panel. **e**, Cleavage assays of the Ago2–Hsp90 system (supplemented with 21 nt siRNA duplex) on a FAM-labeled guide RNA Target. Reactions were performed in cleavage assay buffer at 30 °C, with or without Dicer-2, Dicer-2–R2D2, or Dicer-2–Loqs-PD (bottom panel). Quantified

799 cleavage efficiencies are shown in the top panel. Error bars denote standard deviation
800 (SD) from three independent experiments. Normalization was conducted using the
801 Dicer-2–R2D2 condition as the reference, and all comparisons between this group and
802 others were statistically significant ($P < 0.0001$).
803
804

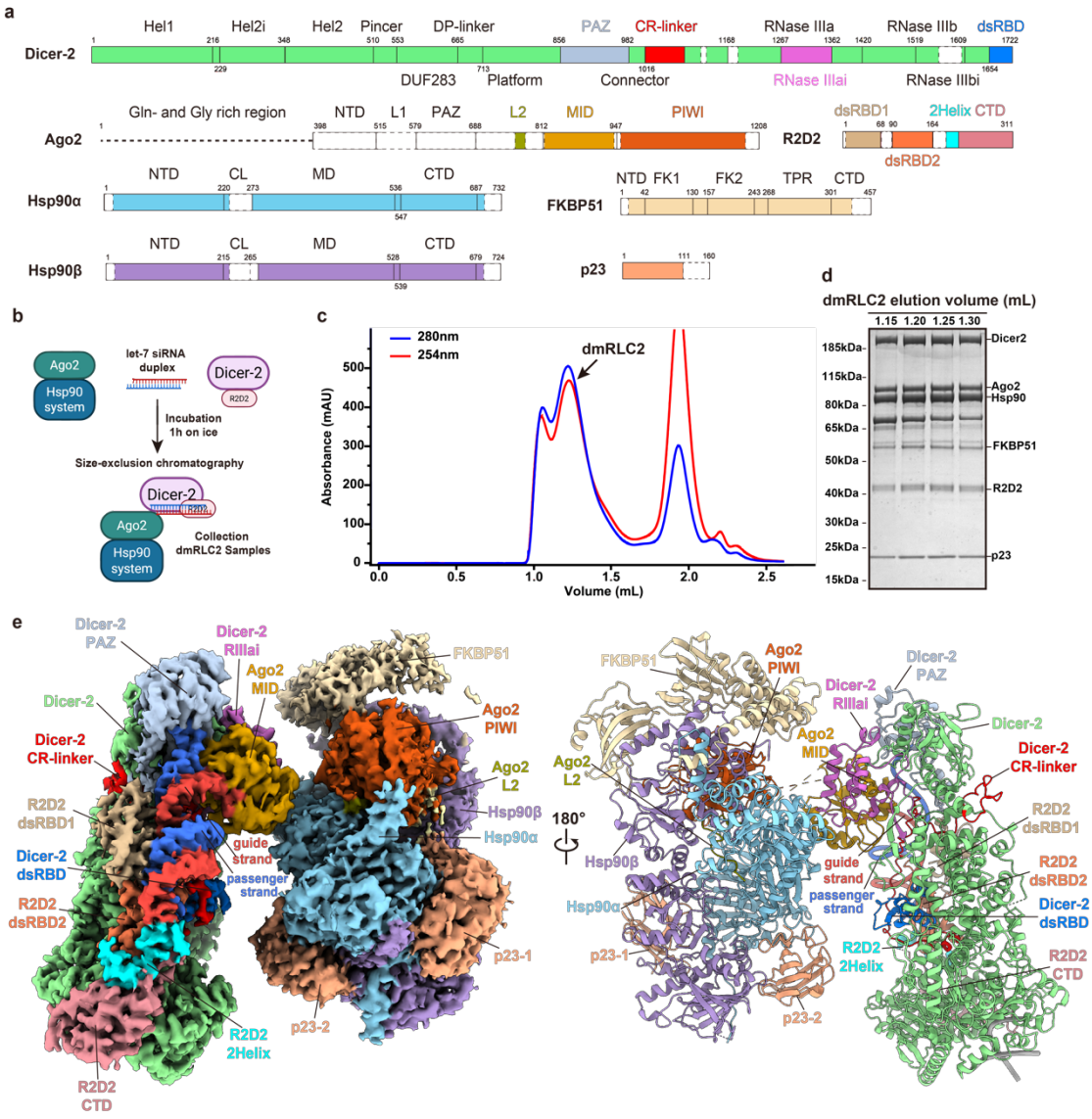

Fig. 2| Cryo-EM structure of the dmRLC2. **a**, Schematic domain architecture of dmRLC2 components: Dicer-2, R2D2, Ago2, Hsp90α, Hsp90β, FKBP51, and p23. Disordered regions are depicted by dashed lines. **b**, Workflow schematic illustrating the preparation procedure for dmRLC2 samples. **c**, Size-exclusion chromatography profile of dmRLC2 assembled from the purified Ago2–Hsp90 system complex, Dicer-2–R2D2, and let-7 siRNA duplex. **d**, SDS-PAGE analysis of protein fractions obtained from the size-exclusion chromatography shown in **c**. **e**, Overall cryo-EM density map and corresponding cartoon representation of dmRLC2. Color coding is consistent with that used in **a**.

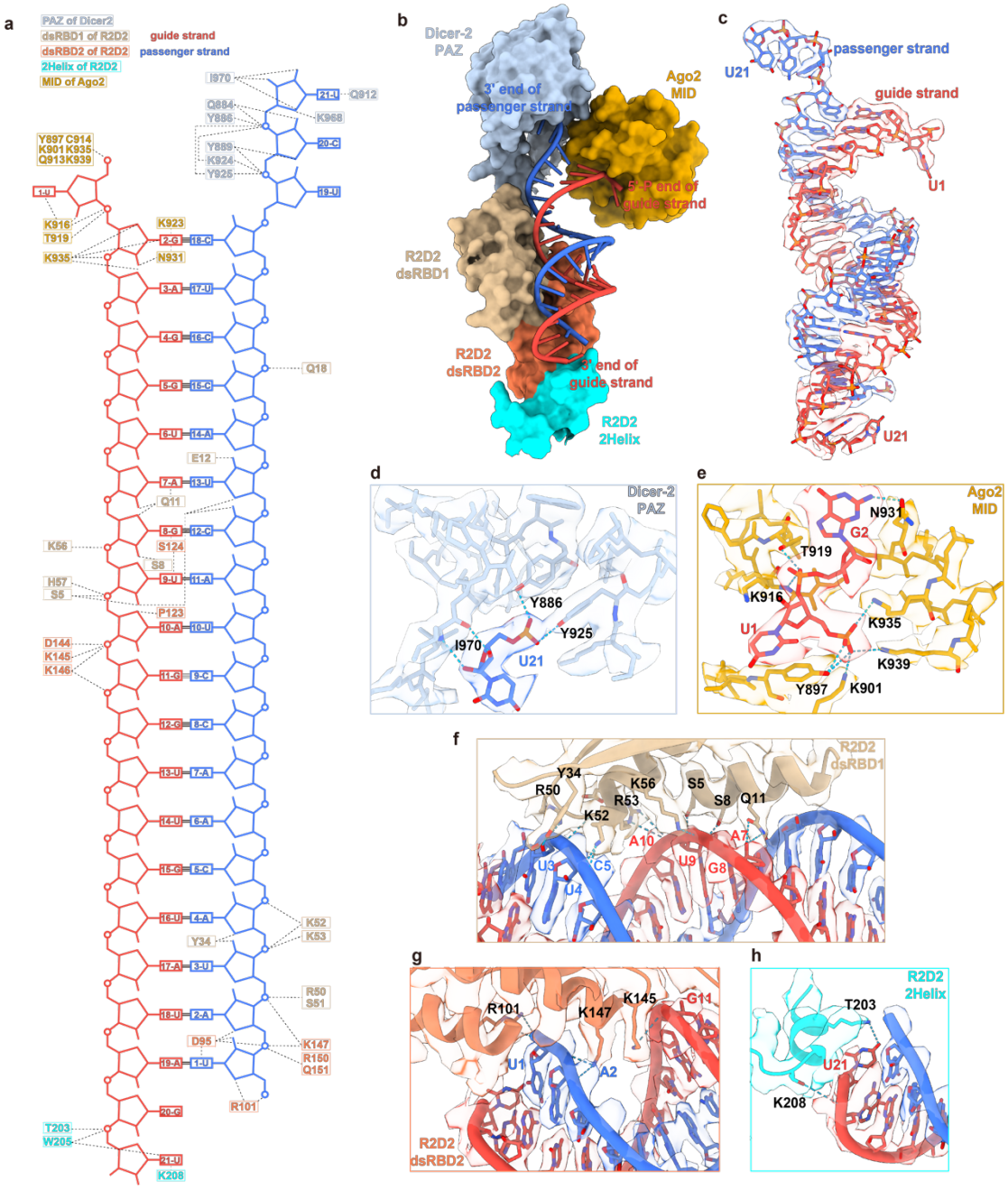

Fig. 3| Protein-nucleic acid interactions in dmRLC2. a, Schematic summary of protein–nucleic acid interactions within dmRLC2 at a distance cutoff of 4 Å, involving Dicer-2, R2D2, and Ago2. Black dashed lines denote interactions between RNA and protein, while black solid lines indicate Watson–Crick base pairs. **b**, Overall architecture of the siRNA duplex bound by the PAZ domain of Dicer-2, the MID domain of Ago2, and the dsRBD1, dsRBD2, and 2Helix regions of R2D2. RNA is depicted as a cartoon; proteins are shown in surface representation. **c**, Atomic model of the let-7 siRNA duplex fitted into the dmRLC2 cryo-EM density map. The cryo-EM

density is shown as a transparent surface, with the superimposed atomic model displayed as sticks. **d**,**e**, Recognition of the 3′ end of the passenger strand by the 3′-end-binding pocket of the Dicer-2 PAZ domain (**d**) and recognition of the 5′ end of the guide strand by the 5′-end-binding pocket of the Ago2 MID domain (**e**). Key hydrogen bonds are indicated. **f**-**h**, Interactions between the let-7 siRNA duplex and the dsRBD1 (**f**), dsRBD2 (**g**), and 2Helix region (**h**) of R2D2. Cryo-EM density maps are shown as transparent surfaces; atomic models and interacting residues are depicted as sticks with heteroatom coloring.

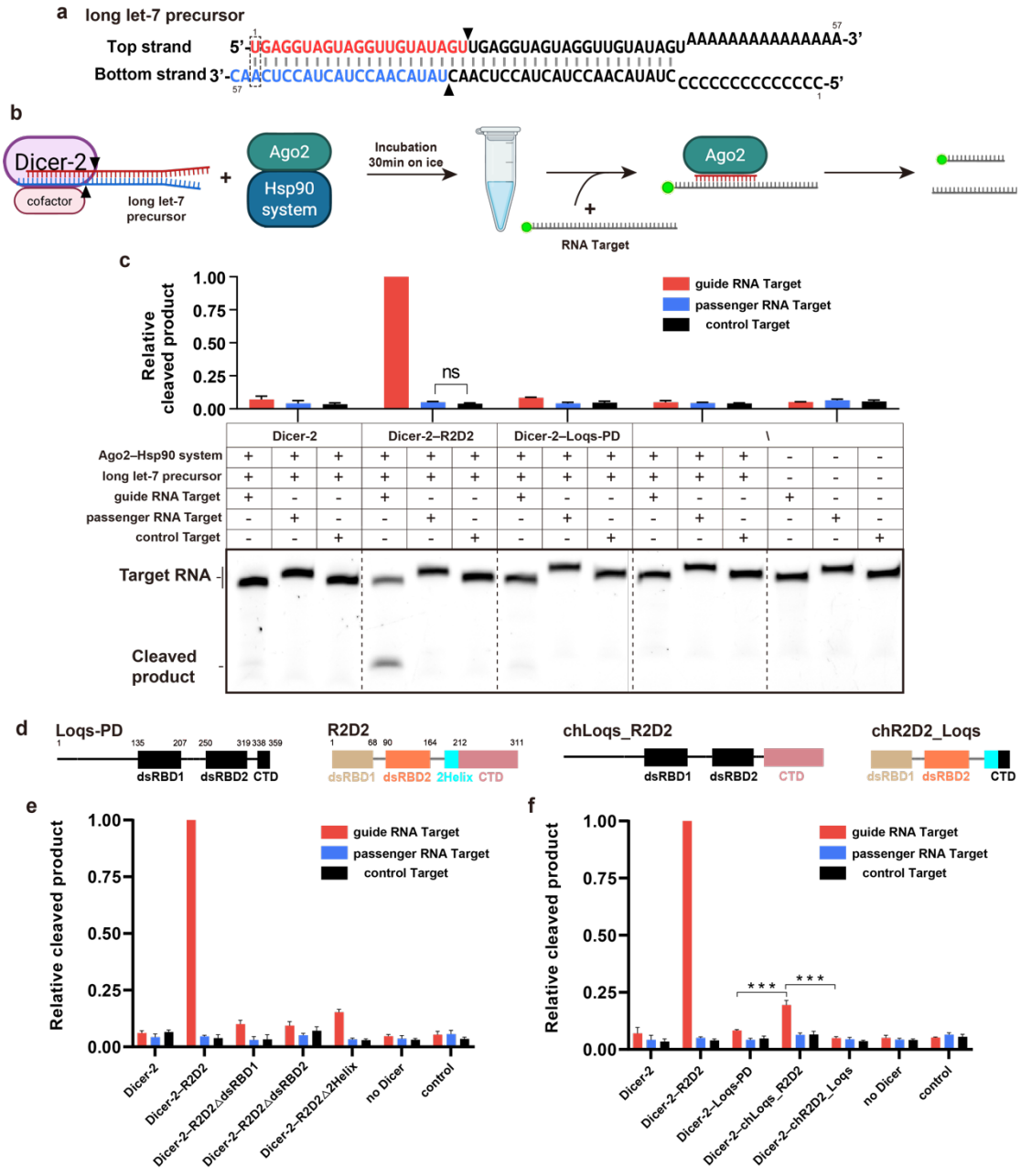

Fig. 4| Guide strand selection in the dmRLC2 and the functional mode of R2D2 dsRBDs. a, Nucleotide sequence of the 57-nt long let-7 precursor. Dicer-2 processes this precursor to generate a 21-nt let-7 duplex analog featuring a fully complementary stem and lacking significant thermodynamic asymmetry between its two termini. Black triangles indicate the Dicer-2 dicing sites. The dashed box highlights base-pairing differences compared to the let-7 siRNA duplex. **b**, Schematic illustration of the cleavage assay workflow. **c**, Cleavage assays of the Ago2–Hsp90 system supplemented with the long let-7 precursor, evaluated using FAM-labeled guide RNA Target,

passenger RNA Target, or control Target. Reactions were performed in cleavage assay buffer at 30 °C, with or without Dicer-2, Dicer-2–R2D2, or Dicer-2–Loqs-PD (bottom panel). Quantified cleavage efficiencies are shown in the top panel. **d**, Schematic domain architectures of Loqs-PD, R2D2, and the chimeric mutants chLoqs_R2D2 and chR2D2_Loqs. **e**, Quantification of cleavage assays using FAM-labeled guide RNA Target, passenger RNA Target, or control Target. Reactions included Dicer-2 alone, Dicer-2–R2D2, or Dicer-2 combined with R2D2 truncation mutants, in the presence of the long let-7 precursor (related to Extended Data Fig. 9b). **f**, Quantification of cleavage assays using FAM-labeled guide RNA Target, passenger RNA Target, or control Target. Reactions included Dicer-2 alone, Dicer-2–R2D2, Dicer-2–Loqs-PD, or Dicer-2 combined with chimeric mutants, in the presence of the long let-7 precursor (related to Extended Data Fig. 10b). Error bars represent standard deviation (SD) from three independent experiments. Normalization was performed using the Dicer-2–R2D2 group with the guide RNA Target as the reference. All statistical comparisons between this group and others were highly significant ($P < 0.0001$). Statistical significance is denoted as follows: ns, $P > 0.05$; ***, $P < 0.001$.

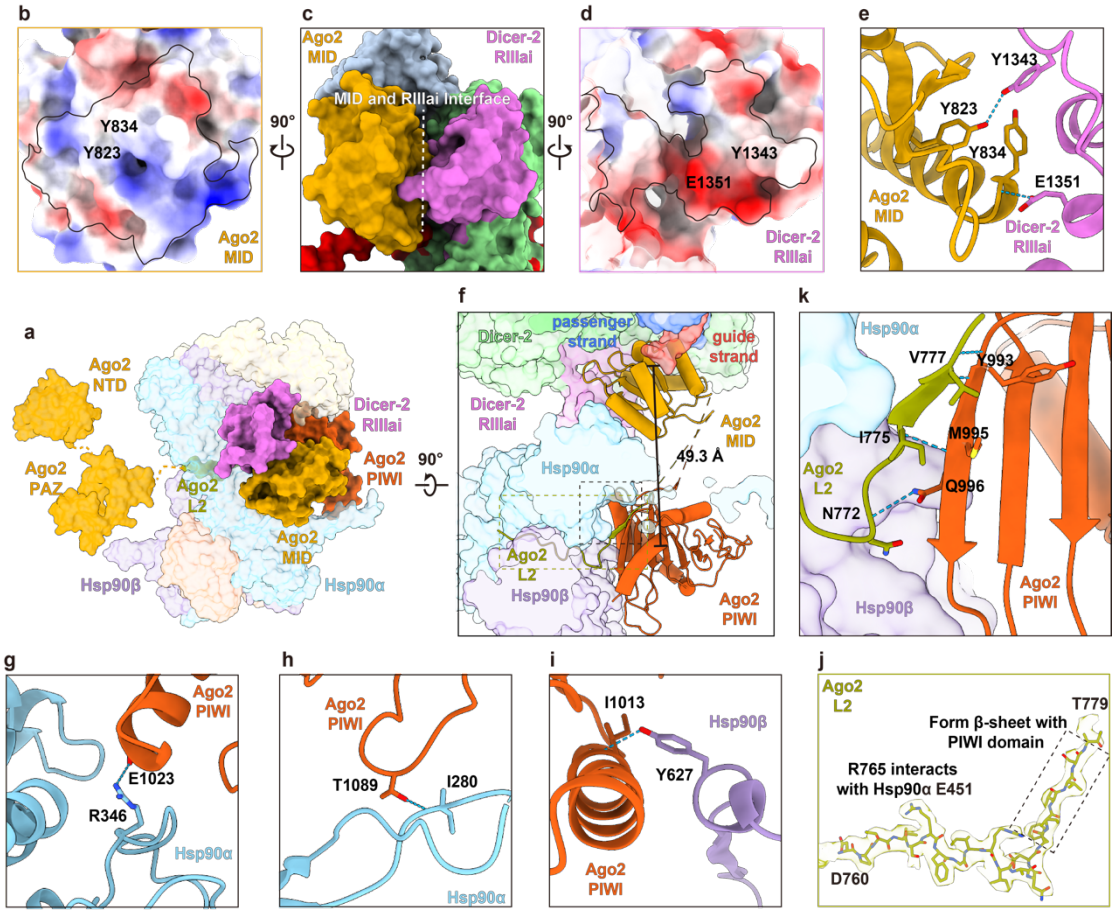

Fig. 5| Interactions mediated by Ago2 in the dmRLC2. a, Spatial organization of Ago2 domains in relation to the Hsp90 system and the RIIIai domain of Dicer-2. The cryo-EM density corresponding to the Hsp90 system, the Dicer-2 RIIIai domain, and the unmodeled region of Ago2 is shown as a transparent surface, whereas the built atomic model of Ago2 is depicted as a solid surface. **b-d,** Detailed view of the interface (**c**) between the Ago2 MID domain (**b**) and the Dicer-2 RIIIai domain (**d**). Both domains are shown as electrostatic potential surfaces, with black lines delineating regions involved in electrostatic interactions. The white dashed line outlines the overall interaction interface (**c**). **e**, Hydrogen-bonding interactions between the Dicer-2 RIIIai domain and the Ago2 MID domain. Residues participating in these interactions are shown as sticks. **f**, Spatial arrangement of the L2, PIWI, and MID domains within Ago2. The cryo-EM density for the Hsp90 system, Dicer-2, and the let-7 siRNA duplex is shown as a transparent surface, with Ago2 represented as a cartoon. The olive dashed box is magnified in (**j**), and the black dashed box in (**k**). **g-i**, Hydrogen-bonding

interactions between Hsp90α (**g** and **h**) or Hsp90β (**i**) and the Ago2 PIWI domain. Interacting residues are shown as sticks. **j**, Atomic model of the Ago2 L2 region (residues D760 to T779) fitted into the dmRLC2 cryo-EM density map. The dashed box highlights the region that functionally interacts with the Ago2 PIWI domain. Cryo-EM density is shown as a transparent surface, with the superimposed atomic model displayed as sticks. **k**, Hydrogen-bonding interactions between the PIWI domain and the L2 region of Ago2. The cryo-EM density for the Hsp90 system is shown as a transparent surface; the PIWI domain and L2 region are depicted as cartoons.

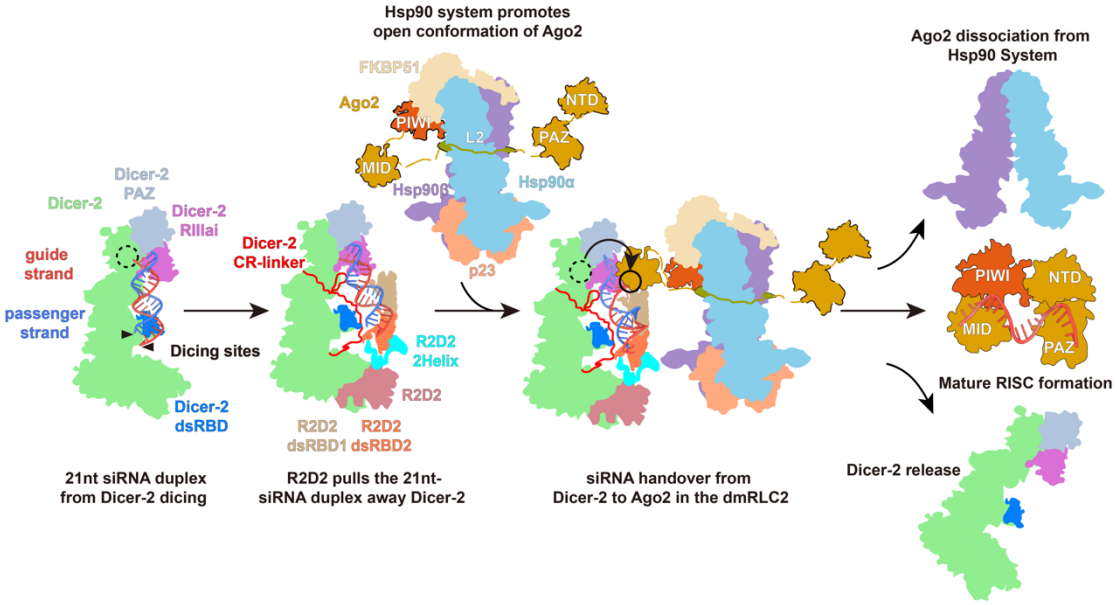

887

888 **Fig. 6| Model for siRNA handover from Dicer-2 to Ago2.** Dicer-2 processes a
889 precursor dsRNA to generate a 21-nt siRNA duplex. During cleavage, the end of the
890 RNA distal to the catalytic site is anchored such that its 5'-end binds to the pocket
891 formed by the Platform domain, and its 3'-end engages the pocket of the PAZ domain.
892 Subsequently, the dsRBDs of R2D2 bind the end proximal to the catalytic center and
893 pull the duplex outward, positioning it in a conformation that projects away from Dicer-
894 2. Concurrently, the Hsp90 system remodels cytosolic Ago2 into an open conformation,
895 dividing it into two modules - one comprising the NTD and PAZ domain, the other
896 containing the MID and PIWI domains - thereby establishing a competent state for
897 RNA loading. Upon association of the Dicer-2–R2D2–siRNA complex with the Ago2–
898 Hsp90 system, the MID domain of Ago2 interacts with the RIIIai domain of Dicer-2.
899 This interaction facilitates a pronounced reorientation: the 5'-end of the siRNA duplex,
900 initially bound to the Platform domain, flips out and is captured by the 5'-end binding
901 pocket within the Ago2 MID domain. The strand bearing this 5'-end is thereby selected
902 as the guide strand during RISC maturation. Subsequently, the Hsp90 dimer dissociates,
903 releasing Ago2. The two modules of Ago2 then reorient and close around the siRNA
904 duplex to form a stable complex. This conformational transition is coupled with the
905 ejection of the passenger strand, ultimately yielding a functional, mature RISC.

906

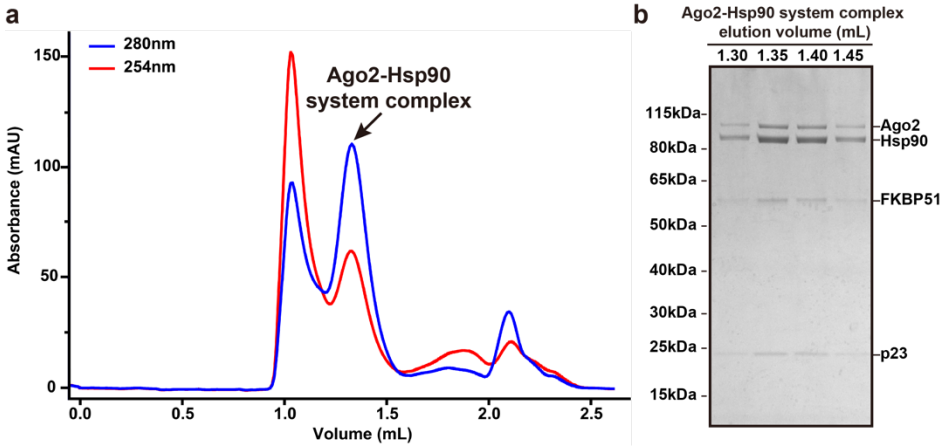

907

908 **Extended Data Fig. 1| Purification of the Ago2–Hsp90 system complex. a**, Size-
909 exclusion chromatography profile of the Ago2–Hsp90 system complex. **b**, SDS-PAGE
910 analysis of the protein fractions obtained from the size-exclusion chromatography
911 shown in (**a**).

912

913

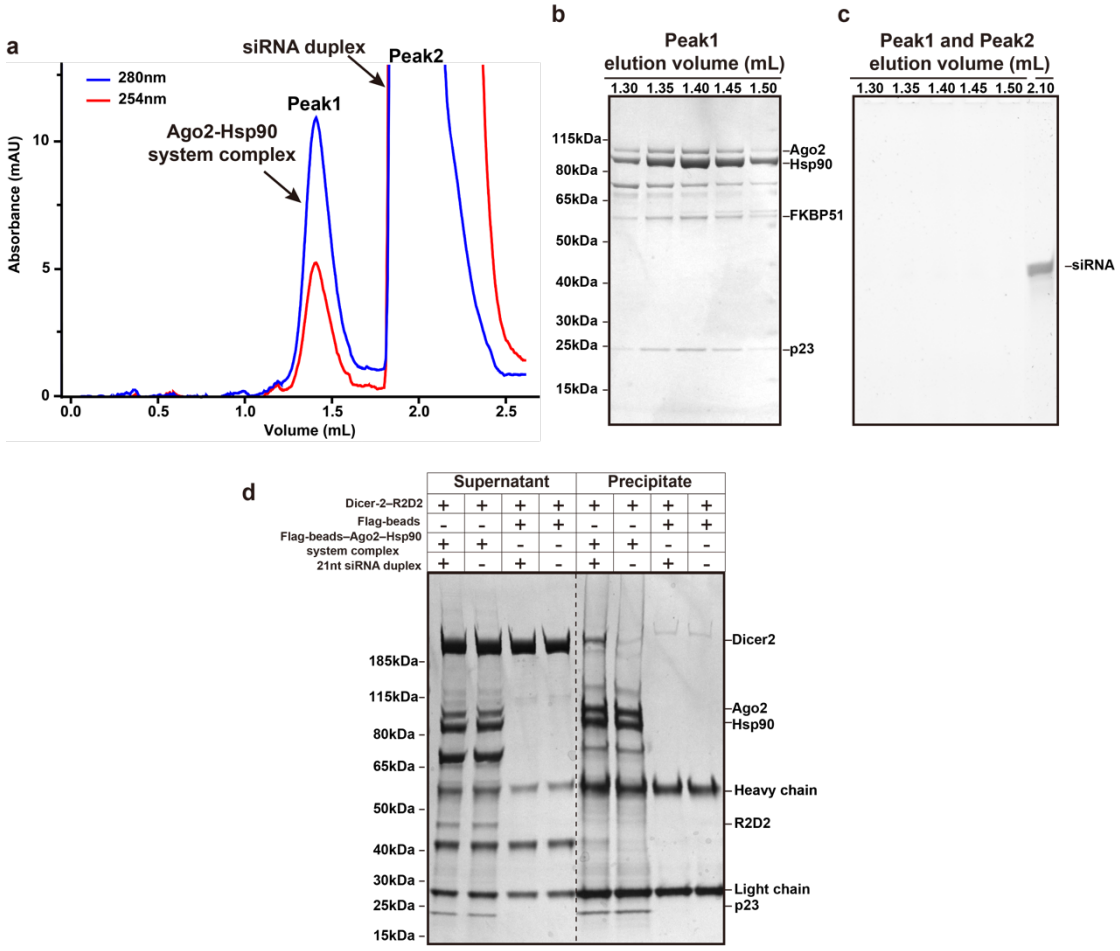

Extended Data Fig. 2| Analysis of the Ago2–Hsp90 system complex assembly with RNA substrates. a, Size-exclusion chromatography profile of the Ago2–Hsp90 system complex after incubation with the let-7 siRNA duplex. **b**,**c**, SDS-PAGE analysis (**b**) and 15% denaturing urea-PAGE analysis (**c**) of the peak fractions collected from the size-exclusion chromatography shown in (**a**). **d**, SDS-PAGE analysis of a pulldown assay demonstrating that the Ago2–Hsp90 complex immobilized on Flag beads recruits Dicer-2–R2D2 from solution, in both the presence and absence of the let-7 siRNA duplex.

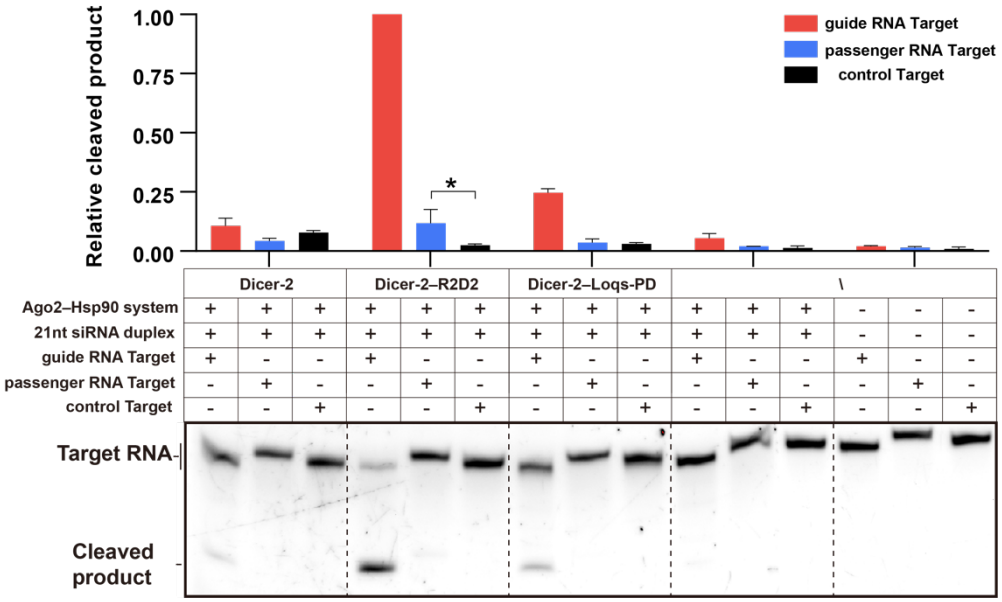

925

926 **Extended Data Fig. 3| RNA-processing activities supported by Dicer-2 and its**
927 **cofactors.** Cleavage assays of the Ago2–Hsp90 system supplemented with a 21 nt let-
928 7 siRNA duplex, evaluated using FAM-labeled guide RNA Target, passenger RNA
929 Target, or control Target. Reactions were performed in cleavage assay buffer at 30 °C,
930 with or without Dicer-2, Dicer-2–R2D2, or Dicer-2–Loqs-PD (bottom panel).
931 Quantified cleavage efficiencies are shown in the top panel. Error bars represent the
932 standard deviation (SD) from three independent experiments. Normalization was
933 performed using the Dicer-2–R2D2 group with the guide RNA Target as the reference.
934 All statistical comparisons between this group and others were highly significant ($P < 0.0001$). Statistical significance is denoted as follows: *, $P < 0.05$.

936

937

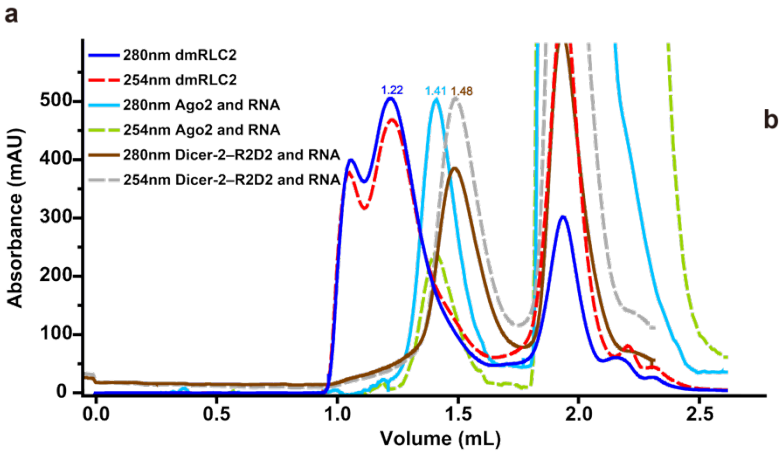

b

System	UV254/UV280
dmRLC2	0.93
Ago2+RNA	0.48
Dicer-2–R2D2+RNA	1.33

Extended Data Fig. 4| Assembly of the dmRLC2. a, Comparison of size-exclusion chromatography profiles of the fully assembled dmRLC2 complex - comprising the Ago2–Hsp90 system complex, Dicer-2–R2D2, and the let-7 siRNA duplex - alongside two control samples: the Dicer-2–R2D2–siRNA duplex complex, and the mixture of the Ago2–Hsp90 system complex incubated with the siRNA duplex alone. **b**, UV absorbance ratios (254 nm/280 nm) corresponding to the peak fractions from the size-exclusion chromatography runs shown in (**a**).

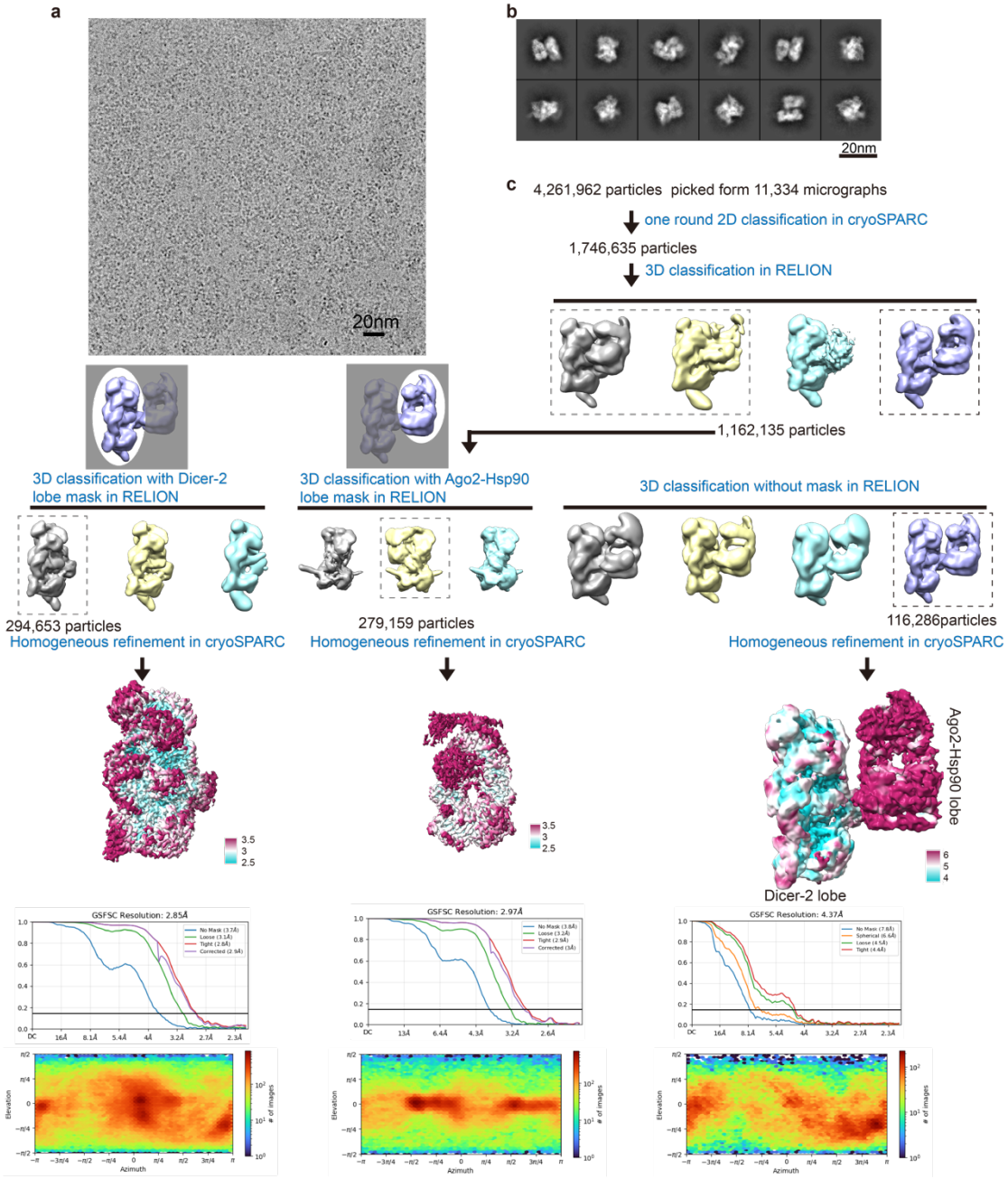

Extended Data Fig. 5| Cryo-EM image processing details of the dmRLC2. a,**b**, Representative cryo-EM micrograph (**a**) and 2D class averages (**b**) of dmRLC2. **c**, Workflow for cryo-EM data processing of dmRLC2. The gold-standard Fourier shell correlation (GSFSC) curve for the final map, angular particle distribution, and final density map colored by local resolution are also shown.

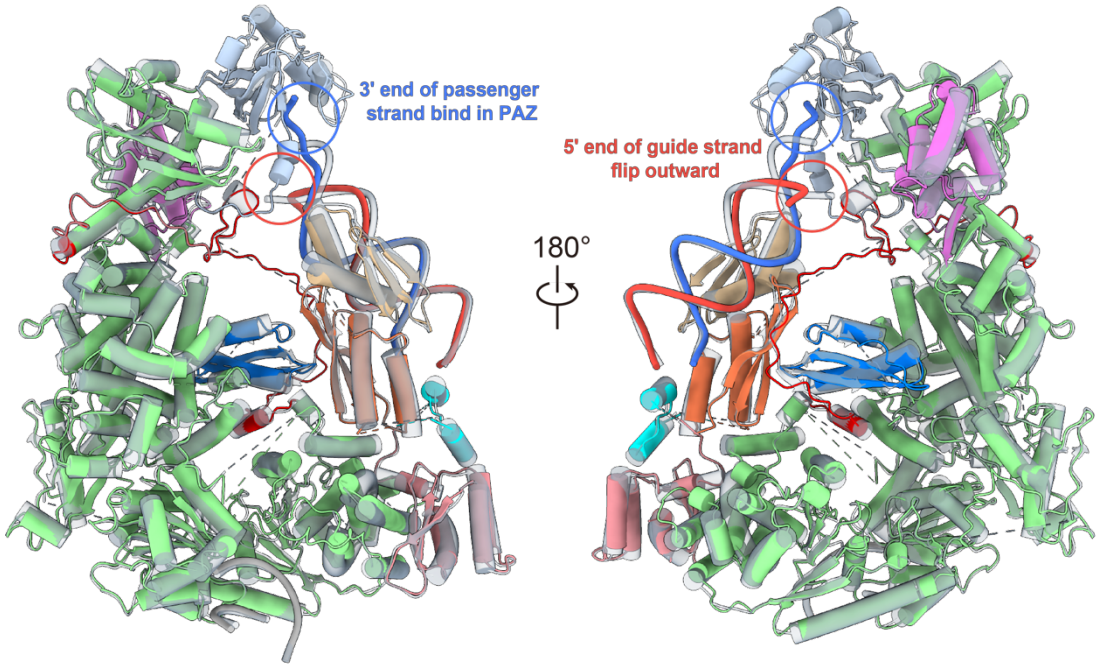

Extended Data Fig. 6| Comparison of the Dicer-2–R2D2–siRNA duplex module in the dmRLC2. Superposition of the Dicer-2–R2D2–siRNA complex (PDB: 7V6C) and the Dicer-2–R2D2–siRNA duplex module within our dmRLC2 structure[46]. The Dicer-2–R2D2–siRNA complex (PDB: 7V6C) is shown as a transparent gray surface.

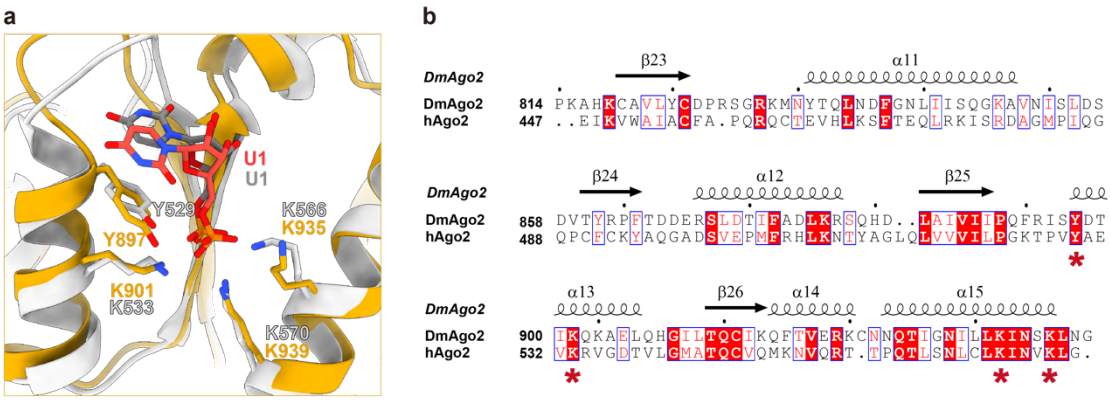

963

964 **Extended Data Fig. 7| Comparison of the 5′-end binding pocket in the Ago2 MID**
965 **domain. a**, Superimposition of the interactions between the 5′-end binding pocket of
966 the Ago2 MID domain and U1 in human RISC (hRISC, PDB: 4W5N) and our dmRLC2
967 structure. The MID domain and U1 in hRISC are shown in gray[63]. **b**, Sequence
968 alignment of the MID domains from hAgo2 and DmAgo2. The secondary structure of
969 DmAgo2 is shown at the top. Conserved residues in the MID domain that mediate
970 interactions with the guide strand RNA are marked with red asterisks. Dm, *Drosophila*
971 *melanogaster*; h, *Homo sapiens*.

972

973

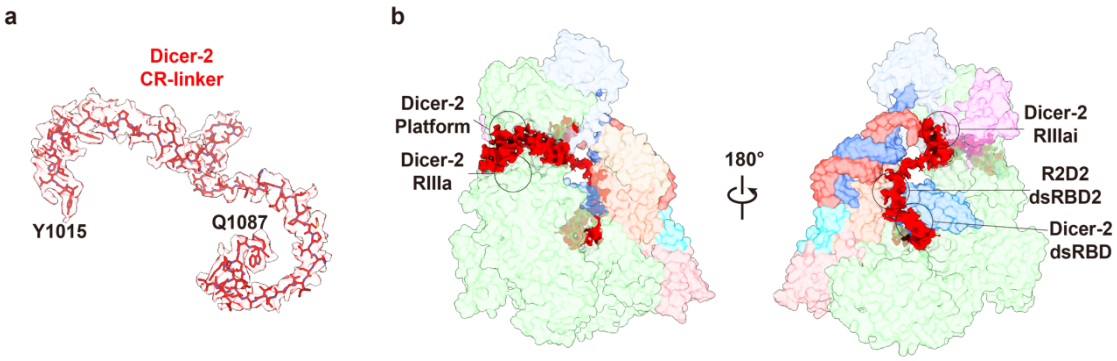

974

975 **Extended Data Fig. 8| Localization of the CR-linker in Dicer-2. a**, Atomic model of
976 the CR-linker region (residues Y1015–Q1087) fitted into the dmRLC2 cryo-EM
977 density map. The density is shown as a transparent surface, with the superimposed
978 atomic model depicted as sticks. **b**, Localization and interaction of the CR-linker region
979 (residues Y1015–Q1087) within dmRLC2. This region contacts the Platform, RIIIa,
980 RIIIai, and dsRBD domains of Dicer-2, as well as the dsRBD2 domain of R2D2. Dicer-
981 2–R2D2 and the let-7 siRNA duplex are rendered as transparent surfaces, while the CR-
982 linker region is highlighted by its cryo-EM density map.

983

984

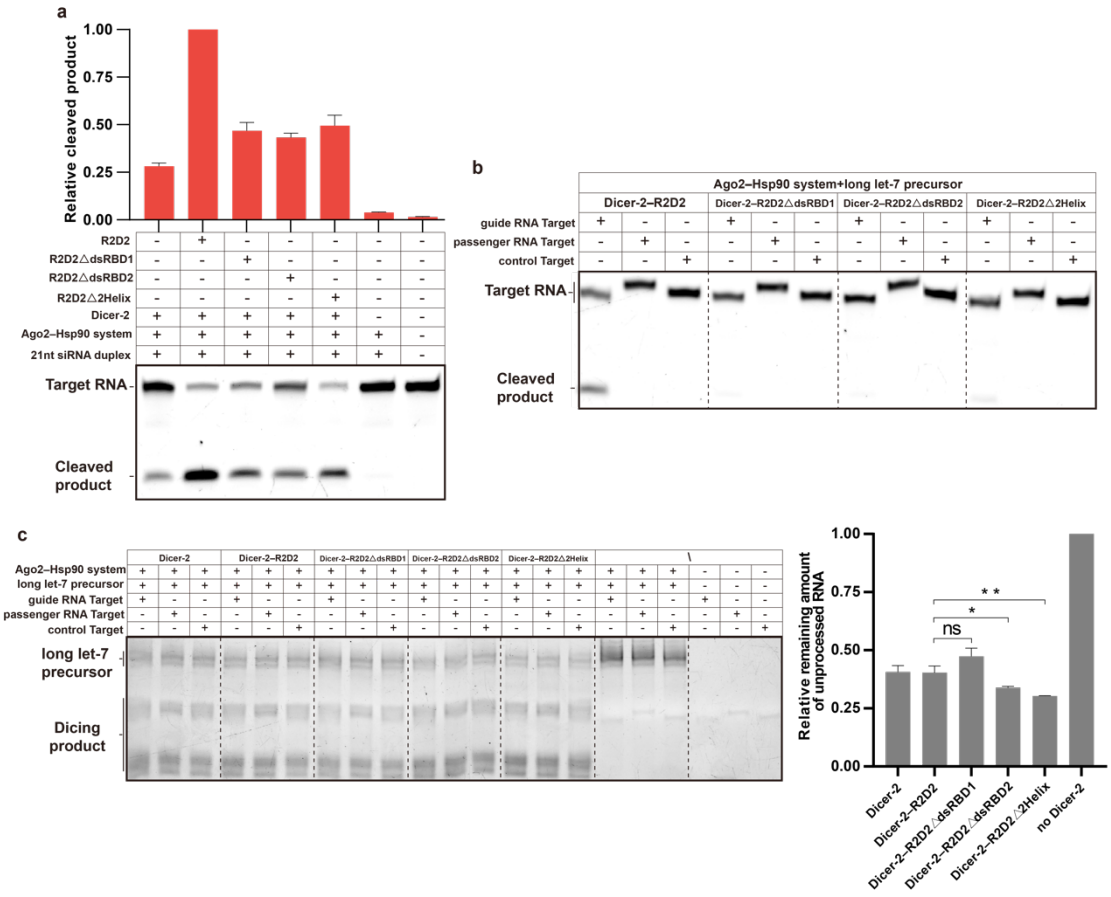

985

986 **Extended Data Fig. 9| RNA-processing activities supported by Dicer-2 with R2D2**
987 **or its truncation mutants. a**, Cleavage assays of the Ago2–Hsp90 system
988 supplemented with a 21 nt let-7 siRNA duplex, evaluated using a FAM-labeled guide
989 RNA Target. Reactions were performed in cleavage assay buffer at 30 °C in the
990 presence or absence of Dicer-2, Dicer-2–R2D2, or Dicer-2 combined with R2D2
991 truncation mutants (bottom panel). Quantified cleavage efficiencies are shown in the
992 top panel. Normalization was performed relative to the Dicer-2–R2D2 group. All
993 statistical comparisons between this group and others were highly significant ($P <$
994 0.0001). **b**, Cleavage assays of the Ago2–Hsp90 system supplemented with the long
995 let-7 precursor RNA, evaluated using FAM-labeled guide RNA Target, passenger RNA
996 Target, or control Target. Reactions were performed in cleavage assay buffer at 30 °C
997 in the presence of Dicer-2–R2D2 or Dicer-2 combined with R2D2 truncation mutants.
998 **c**, Dicing assays using the long let-7 precursor as substrate, performed with Dicer-2
999 alone or in complex with R2D2 or its truncation mutants, under the same conditions as

in (**b**) (left panel). Quantified dicing efficiencies are shown on the right. Error bars represent standard deviation (SD) from three independent experiments. Normalization was performed relative to the no-Dicer-2 control group. Statistical significance is denoted as follows: ns, $P > 0.05$; *, $P < 0.05$; **, $P < 0.01$.

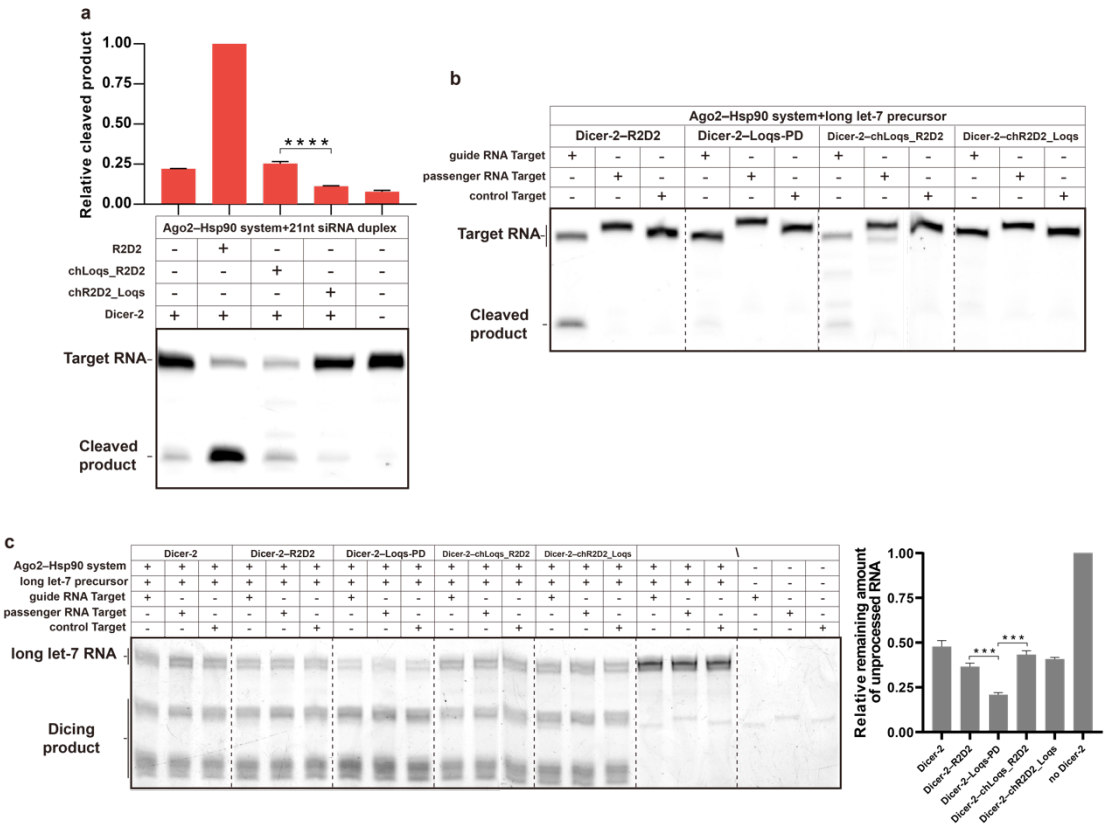

Extended Data Fig. 10| RNA-processing activities supported by Dicer-2 with cofactors or its mutants. a, Cleavage assays of the Ago2–Hsp90 system supplemented with a 21 nt let-7 siRNA duplex, evaluated using a FAM-labeled guide RNA Target. Reactions were performed in cleavage assay buffer at 30 °C in the presence or absence of Dicer-2, Dicer-2–R2D2, or Dicer-2 combined with the chimeric mutants chLoqs_R2D2 or chR2D2_Loqs (bottom panel). Quantified cleavage efficiencies are shown in the top panel. Normalization was performed relative to the Dicer-2–R2D2 group. All statistical comparisons between this group and others were highly significant ($P < 0.0001$). **b**, Cleavage assays of the Ago2–Hsp90 system supplemented with the long let-7 precursor RNA, evaluated using FAM-labeled guide RNA Target, passenger RNA Target, or control Target. Reactions were performed in cleavage assay buffer at 30 °C in the presence of Dicer-2–R2D2, Dicer-2–Loqs-PD, or Dicer-2 combined with the chimeric mutants. **c**, Dicing assays using the long let-7 precursor as substrate, performed with Dicer-2 alone or in complex with R2D2, Loqs-PD, or the chimeric mutants, under the same conditions as in (**b**) (left panel). Quantified dicing efficiencies are shown on the right. Error bars represent standard deviation (SD) from three

1022 independent experiments. Normalization was performed relative to the no-Dicer-2
1023 control group. Statistical significance is denoted as follows: ***, $P < 0.001$; ****, $P <$
1024 0.0001.
1025
1026

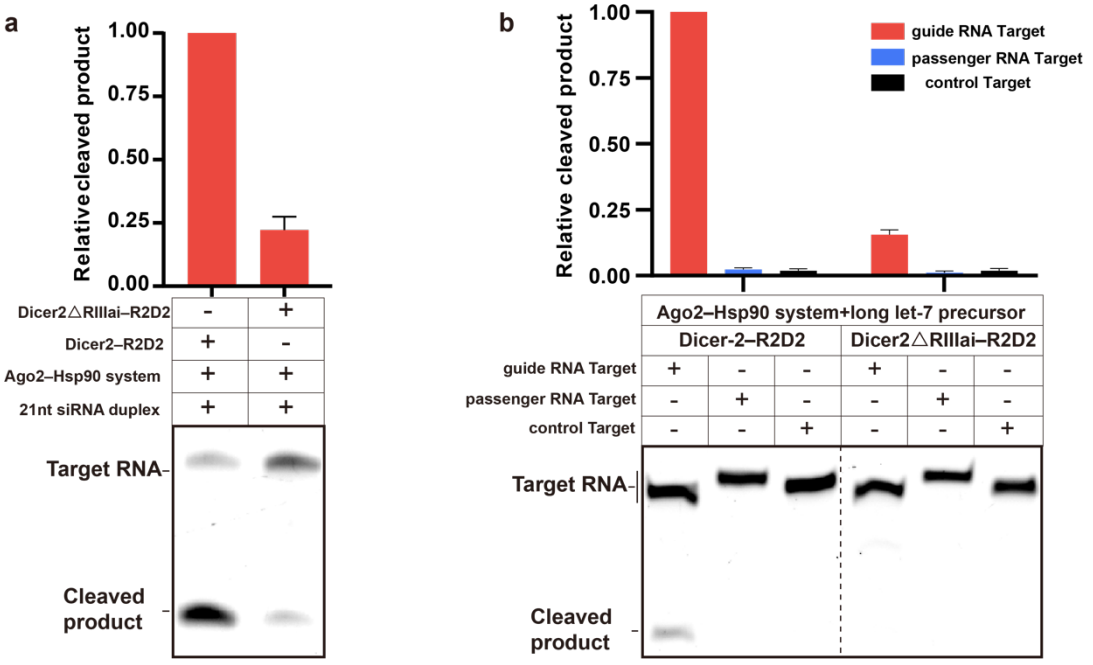

Extended Data Fig. 11| RNA-processing activities supported by Dicer-2 or Dicer-2ΔRIIIai. a, Cleavage assays of the Ago2–Hsp90 system supplemented with a 21 nt let-7 siRNA duplex, evaluated using a FAM-labeled guide RNA Target. Reactions were performed in cleavage assay buffer at 30 °C in the presence of Dicer-2–R2D2 or Dicer-2ΔRIIIai–R2D2 (bottom panel). Quantified cleavage efficiencies are shown in the top panel. Normalization was performed relative to the Dicer-2–R2D2 group, and the difference between this group and the Dicer-2ΔRIIIai–R2D2 group was statistically significant ($P < 0.0001$). **b**, Cleavage assays of the Ago2–Hsp90 system supplemented with the long let-7 precursor RNA, evaluated using FAM-labeled guide RNA Target, passenger RNA Target, or control Target. Reactions were performed in cleavage assay buffer at 30 °C in the presence of Dicer-2–R2D2 or Dicer-2ΔRIIIai–R2D2. Quantified cleavage efficiencies are shown in the top panel. Normalization was performed relative to the Dicer-2–R2D2 group assayed with the guide RNA Target. All statistical comparisons between this group and others were highly significant ($P < 0.0001$).

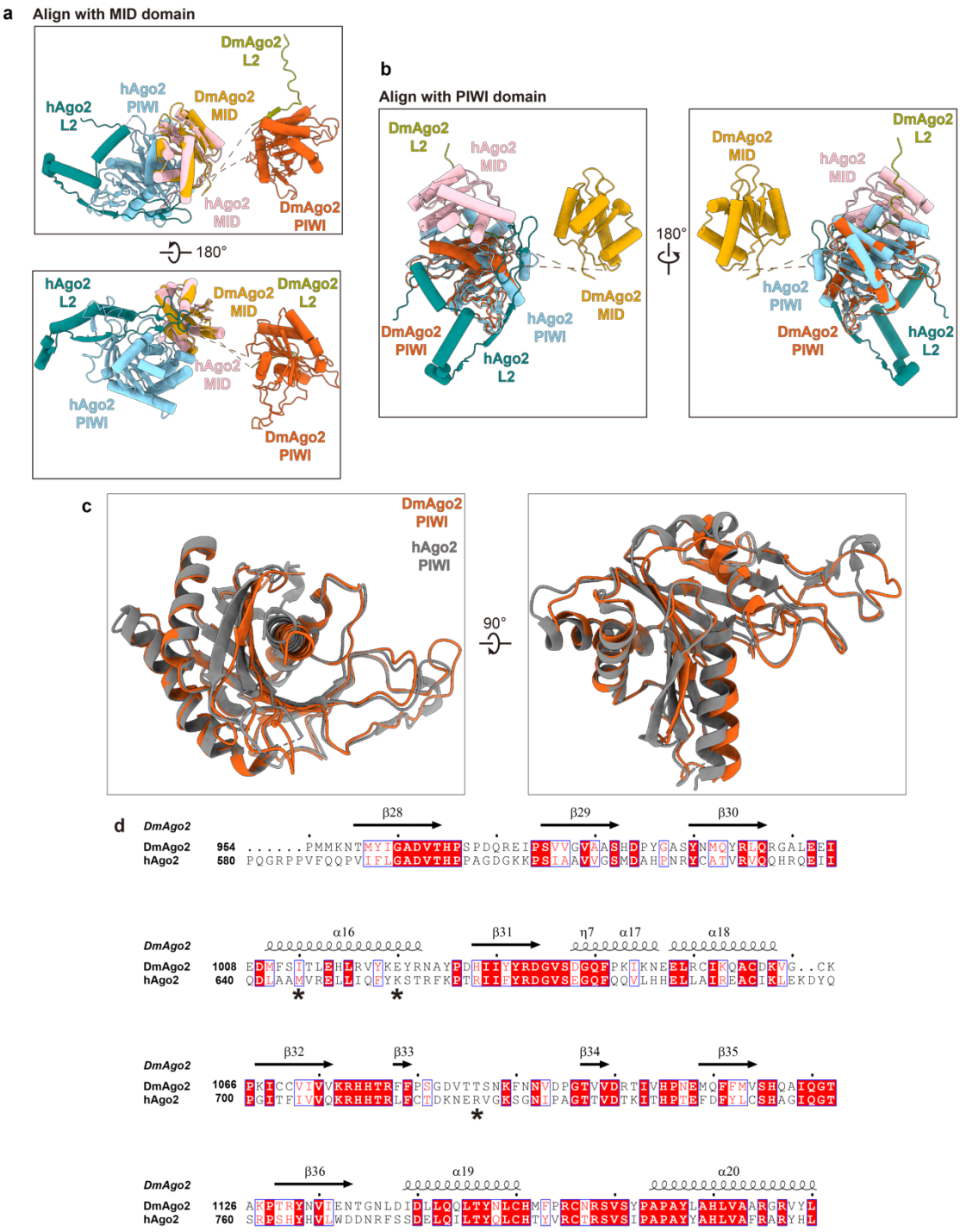

Extended Data Fig. 12| Comparison of the Ago2. a,**b**, Structural superimposition of hAgo2 in human RISC (hRISC, PDB: 4W5N) and DmAgo2 in our dmRLC2. [63]. The models were aligned based on the MID domain (**a**) and the PIWI domain (**b**), respectively. **c**, Superimposition of the PIWI domain in hRISC (PDB: 4W5N, shown in gray) and our dmRLC2 structure. **d**, Sequence alignment of the PIWI domains of hAgo2 and DmAgo2. Residues involved in interactions with Hsp90 proteins are indicated by

1051 black asterisks. The secondary structure elements of DmAgo2 are shown above the
1052 alignment. Dm, *Drosophila melanogaster*; h, *Homo sapiens*.
1053
1054

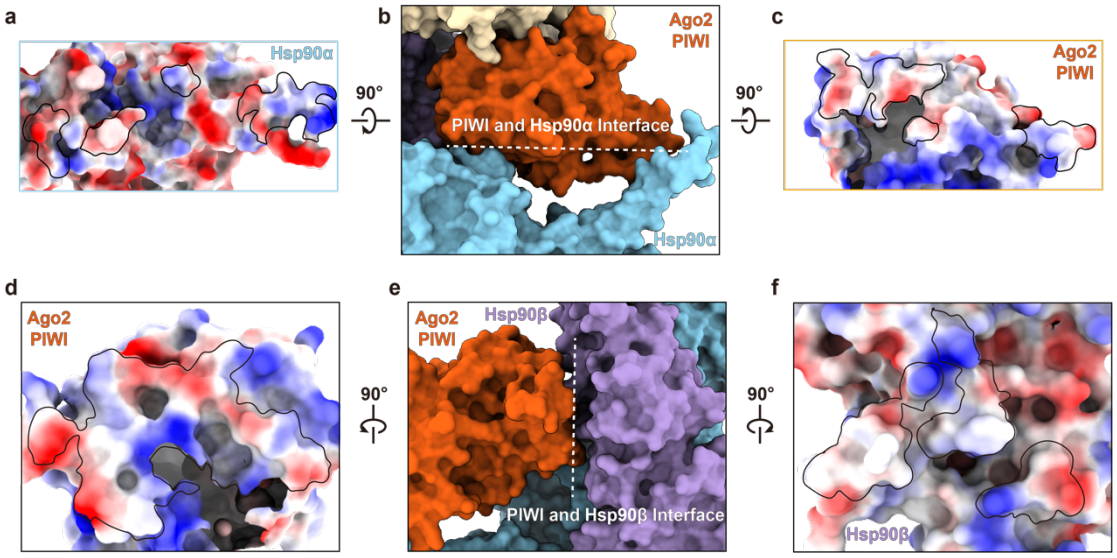

Extended Data Fig. 13| Interaction between the Ago2 PIWI domain and the Hsp90s. a-c, Detailed view of the interface (**b**) between Hsp90α (**a**) and the Ago2 PIWI domain (**c**). **d-f**, Detailed view of the interface (**e**) between the Ago2 PIWI domain (**d**) and Hsp90β (**f**). Hsp90s and the PIWI domain are shown as electrostatic potential surfaces, with black lines delineating regions involved in electrostatic interactions. The white dashed line outlines the overall interaction interface.

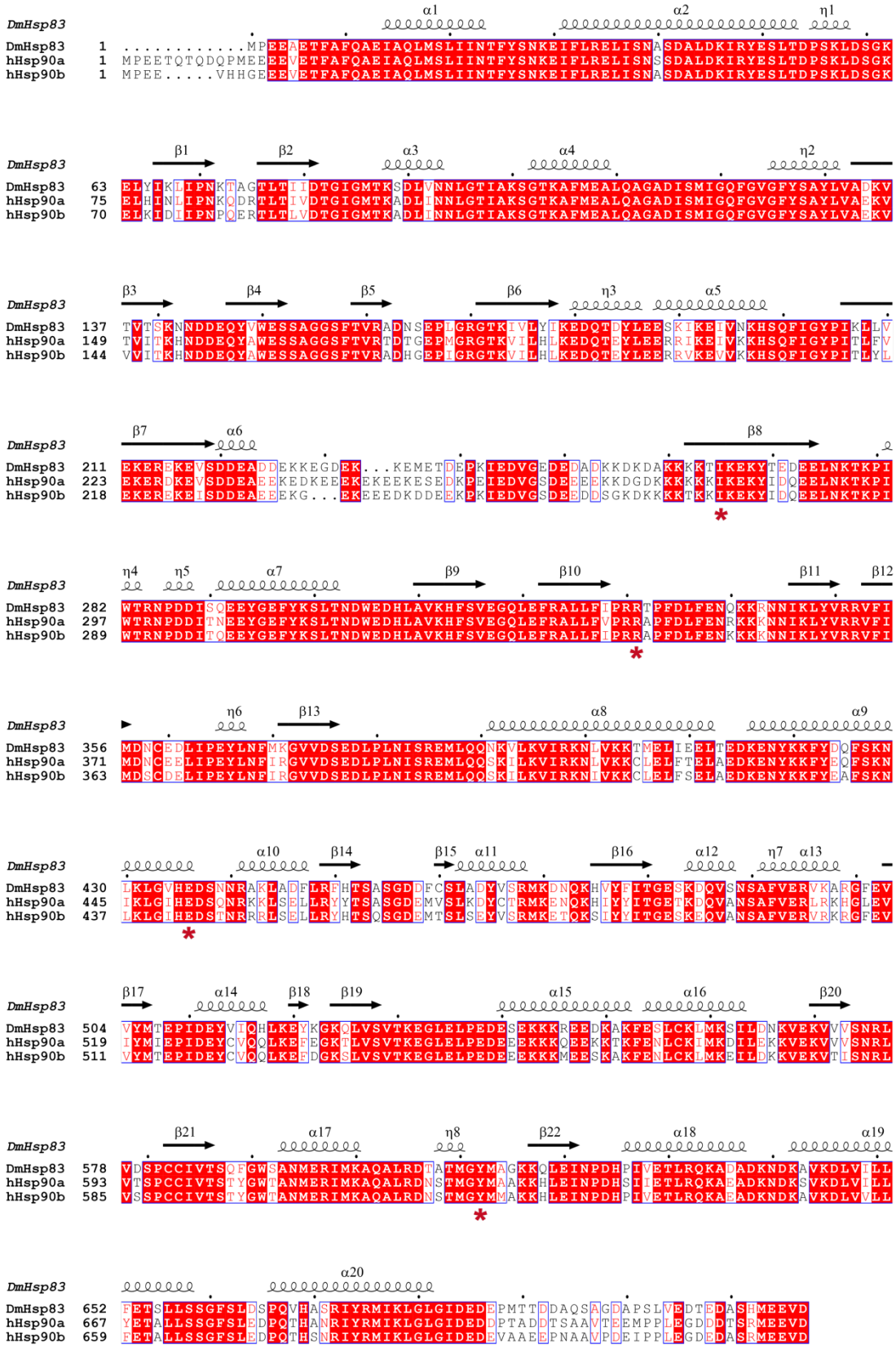

Extended Data Fig. 14| Comparison of the Hsp90. Sequence alignment of DmHsp83, hHsp90α and hHsp90β. Secondary structures of DmHsp83 are shown at the top.

1067 Conserved residues that interact with Ago2 are marked with red asterisks. Dm,
1068 *Drosophila melanogaster*; h, *Homo sapiens*.
1069

1070

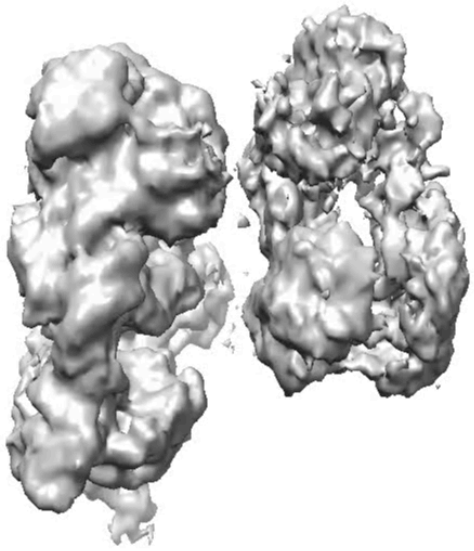

1071 **Extended Data Movie 1|** Conformational flexibility exists between the two lobes in

1072 dmRLC2.

1073

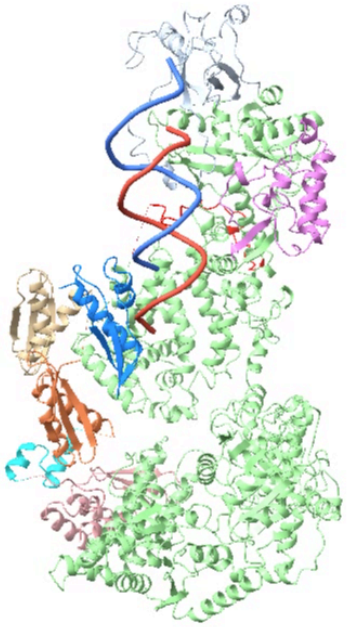

Extended Data Movie 2| In the RNAi pathway, Dicer-2, with the assistance of its cofactors, cleaves and processes dsRNA precursors derived from exogenous viral infections or the genome. Subsequently, the nascent 21-nt siRNA duplexes are transferred to Ago2 by Dicer-2 and its cofactor R2D2, a process regulated by the Hsp90 chaperone system and mediated by the dmRLC2. Ultimately, this enables the loading of siRNA onto Ago2 to form functional, mature RISC.

Extended Data Table 1| Cryo-EM data collection, processing, model refinement and validation statistics.

	Composite of dmRLC2	Consensus of dmRLC2	Dicer-2 lobe (Dicer-2–R2D2–siRNA duplex–Ago2)	Hsp90 system lobe (Hsp90α–Hsp90β–p23–FKBP51–Ago2)
PDB ID	24BO			
EMDB ID	EMD-69434	EMD-69589	EMD-69588	EMD-69587
Data collection and processing				
Microscope		Titan Krios		
Dctector		Falcon 4 with GIF Quantum (20eV silt)		
CS (mm)		2.7		
Normal Magnification		81K		
Pixel size (Å)		0.808		
Electron dost (e^-/Å)		50 (32 frames)		
Defocus range (μm)		-1.5 ~ -2.0		
Micrographs Number		11,334		
Reconstruction				
Software		cryoSPARC, RELION		
Particles picked		4,261,962		
Particles refinement		116,286	294,653	279,159
Symmetry		C1	C1	C1
Resolution (Å)		4.37	2.85	2.97
Sharpening B-factor ($Å^2$)		70.6	99.9	109.2
Refinement				
Model composition				
Number of atoms	35,113			
Protein residues	4,196			
Nucleotides	54			
Ligand (Mg^{2+}, ADP)	2/2			
B factors	Protein: 2.39/254.18/91.63 Nucleotide: 6.06/104.62/51.51			
Bonds RMSD				
Bonds lengths (Å)	0.003			
Bonds angles (°)	0.603			
Validation				
MolProbity score	2.01			
Clash score	6.85			
Rotamer outliers (%)	2.98			
C-beta outliers (%)	NA			
Ramachandran plot				
Favored (%)	96.06			
Allowed (%)	3.82			
outliers (%)	0.12			
Model vs. Data				
CC mask/box	0.74/0.72			